MATERIALS SCIENCE AND ENGINEERING

A Publication of the University of Miskolc

Volume 44, Number 2

CONTENTS

COMPARISON OF THE RECRYSTALLIZED MICROSTRUTURE OF 8006 AND AL1.4SI ALLOY AFTER LOCAL LASER TREATMENT

TAMÁS BUBONYI[1]–ZSUZSANNA BÁNÓCZY[1]–PÉTER BARKÓCZY[1]

LASER treatment is a widely used surface treatment method. An interesting application where LASER treatment controls the recrystallization volume in cold rolled metals. In this article, an EN AW 8006 and Al1.4Si cold rolled aluminum sheets were annealed by LASER treatment, then the microstructures were compared. The scope is the possibilities of the application of this method in case of the mentioned alloys. The study concentrates the comparison of heat affected zones.

Keywords: Aluminum, LASER treatment, Recrystallization

INTRODUCTION

The LASER induced recrystallization was introduced earlier [1]. The processed volume become smaller and smaller with the fast industrial development. The scale of the examinations became smaller and smaller, and the local treatments became industrial standards, and widely used technique. One surface modifying local treatment is the LASER treatment. In this technology the treated area is illuminated by LASER beam, which projects high energy into the material [2].

In case of metals, the introduced energy is so high, the metal can't dissipate that much, thus great heating rates are achievable. The treatment takes very short time, and after it's done, because the good the heat conduction and the small treated area, the cooling rates are also large. It's clearly visible why this method is so popular nowadays, and why it's good for local treatments. It's used for cutting, welding surface tempering [3], surface alloying [4] and for local annealing which will be introduced in this study.

The dislocation density increment of cold rolled sheet metals shows relationship with the extent of deformation. This extent can be counted as the height reduction of the sheets. This means as thinner the sheet, the dislocation density is greater [5]. Atoms in the deformed metals are not in the lowest energy lattice position; therefore, they have an excess energy which called stored energy [6]. In case of high extent of deformation of aluminum alloy sheet, a little excess heat is enough for start the recovery (in case of low alloyed aluminums) and the recrystallization, the two main phase transformation process of annealing [7]. The recovery means, the dislocations are ordered into dislocation walls [8]. During the recovery the hardness of the sheets

---

[1]   Institute of Physical Metallurgy, Metalforming and Nanotechnology, University of Miskolc
     H-3515 Miskolc-Egyetemváros, Hungary
     fembubo@uni-miskolc.hu

drops and subgrains formed inside the deformed grains. While this process cannot observe in the microstructure by optical microscopy, the recrystallization can [9]. During recrystallization, new nuclei forms mainly at the grain boundaries of deformed grains, and it became growing. The greater the extent of deformation, the amount of the new nuclei rises, resulting fine equiaxial microstructure. The other parameter that affects the process is the temperature. Higher temperature means the process can start earlier at the same reduction level, and at higher the temperature, the microstructure is finer [10]. With LASER treatment, the applied heat can be concentrated into a local area, which means not the whole sheet will be recrystallized, resulting a dual phase material. The temperature of the material is could not adjust finely because of the mentioned fast heating and cooling. The parameters of the treatment which can be adjustable is the power of the LASE beam, the velocity of the movement of the beam, and the dislocation density – the thickness of the rolled aluminum sheet. Earlier published, that the border between the cutting and heat treatment by LASER beam is narrow. There is a small technological window where the behavior of the different sheet can be examined.

One problem in the case of aluminum treatment is its surface: it's acts like a perfect mirror and reflects more than 90% of the LASER beam's energy [11]. To solve this problem, it's necessary to use some sort of graphite layer, which changes the surface properties, and the aluminum became treatable with LASER. An earlier study introduced that the surface of the unalloyed aluminum sheets partially melts at all level of LASER beam energy [12]. This study will introduce the behavior and the microstructure of different kind of aluminum alloy sheets and compare the effect of alloying.

EN AW 8006 alloy is widely used in different kind of applications. The high Fe content makes a high ductility of the material, so it is possible to roll thin foils from this material. This contains small amount of manganese to achieve better microstructural properties. Due to the heterogeneous microstructure these foils can be used as functional or structural material instead of packaging. Al1.4Si contains eutectic Si particles, so the hardness of this alloy is higher, the ductility is not so good as the previously introduced 8006 alloy. But the melting point is lower than the wrought alloys, so it is good material for brazing thin sheets. The automotive industry uses the rolled state of this alloy [13].

1. MATERIALS AND METHODS

Two different kind of aluminum alloys are treated by LASER beam. The iron content of the EN AW 8006 is so high that certain amount of Al-AlFe eutectics form during the DC slab casting. Al1.4Si is the same but Al-Si eutectic forms during the crystallization. The nominal compositions are showed by *Table 1*.

Table 1

The compared aluminum alloys composition

	Al	Si	Mn	Fe	Cu	Mg	Zn	Ti
Al1.4Si	97.05	1.4	0.77	0.44	0.18	0.08	0.036	0.02
EN AW 8006	97.8–94.6	0.4	0.1	1.2–2.0	0.1	0.3–1.0	0.1–1.8	–

The DC slabs hot rolled between 510–300 °C to 6mm in case of EN AW 8006 and to 7 mm in case of Al1.4Si. Then the hot rolled sheets rolled to different thickness by cold rolling. Samples were taken at 3.55 mm, 2.33 mm, 1.57 mm in case of EN AW 8006 and at 3.8 mm, 2.55 mm and 1.8 mm in case of Al1.4Si.

The set-up of LASER treatment was introduced earlier. The surface of the aluminum sheets was sprayed by carbon-black than fixed between copper slabs, to increase the heat capacity of the system to minimize the local melting of the treated surface. The surface then irradiated by laser beam at a given power. Nd:YAG 2.7 kW LASER was used. The LASER beam moved with a fixed 500 mm/min velocity *(Figure 1)*. The diameter of the LASER beam was 2 mm. The preliminary studies show a narrow technological window therefore the LASER power adjusted with the thickness of the sheets. Larger than 3 mm 1000 W, between 2 and 3 mm 900 W, between 1,5 and 2 mm 600 W, under 1,5 mm 450 W LASER power was applied.

The treatment was made in two direction related to the rolling. The movement of the LASER beam in one case was parallel to the rolling direction, and perpendicular to it in the other case.
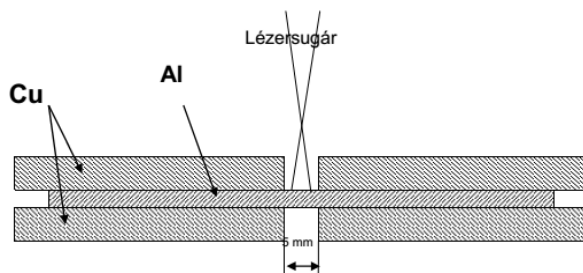

Figure 1
The set-up of the LASER annealing. The alumina sheet fixed between copper slabs the decrease the risk the heat accumulation in the sheet

Samples were taken from the irradiated sheets perpendicular and parallel to the movement of the LASER beam. Metallographic samples prepared for optical microscopic investigation. The samples grinded and polished mechanically. The grinding made by SiC, diamond used as a polishing agent. The polished surface etched by Struers LectroPol electrolytic device with Barker's reagent. The microstructure observed under polarized illumination. The examined area was so large that mosaic image was necessary to make by a Zeiss AxioImager M1m computer controlled optical microscope. The images were evaluated and compared to reveal the effect of the alloying to the microstructure.

2. RESULTS AND DISCUSSION

The microstructures of *Figure 2* show the results of the LASER treatment in case of EN AW 8006 while *Figure 3* shows the same in the case of Al1.4Si. It can be seen of the micrographs, that in all cases a partial melting can be observed. In case of Al1.4Si the size of the molten pool is larger due to the lower melting point. In thin

sheets the pool is as large as the thickness of the sheet. The molten pool is as deep as nearly the half of the sheet thickness at EN AW 8006 alloy sheets, but the extent of the columnar zone is higher. This difference originated that the Al1.4Si is really an alloy for casting, not a real wrought alloy. The constitutional undercooling at aluminum iron alloy is larger. Another general observation that recrystallization occurs at the heat affected zone. The grain size is nearly the same and extra fine compared to the deformed or crystallized grains.
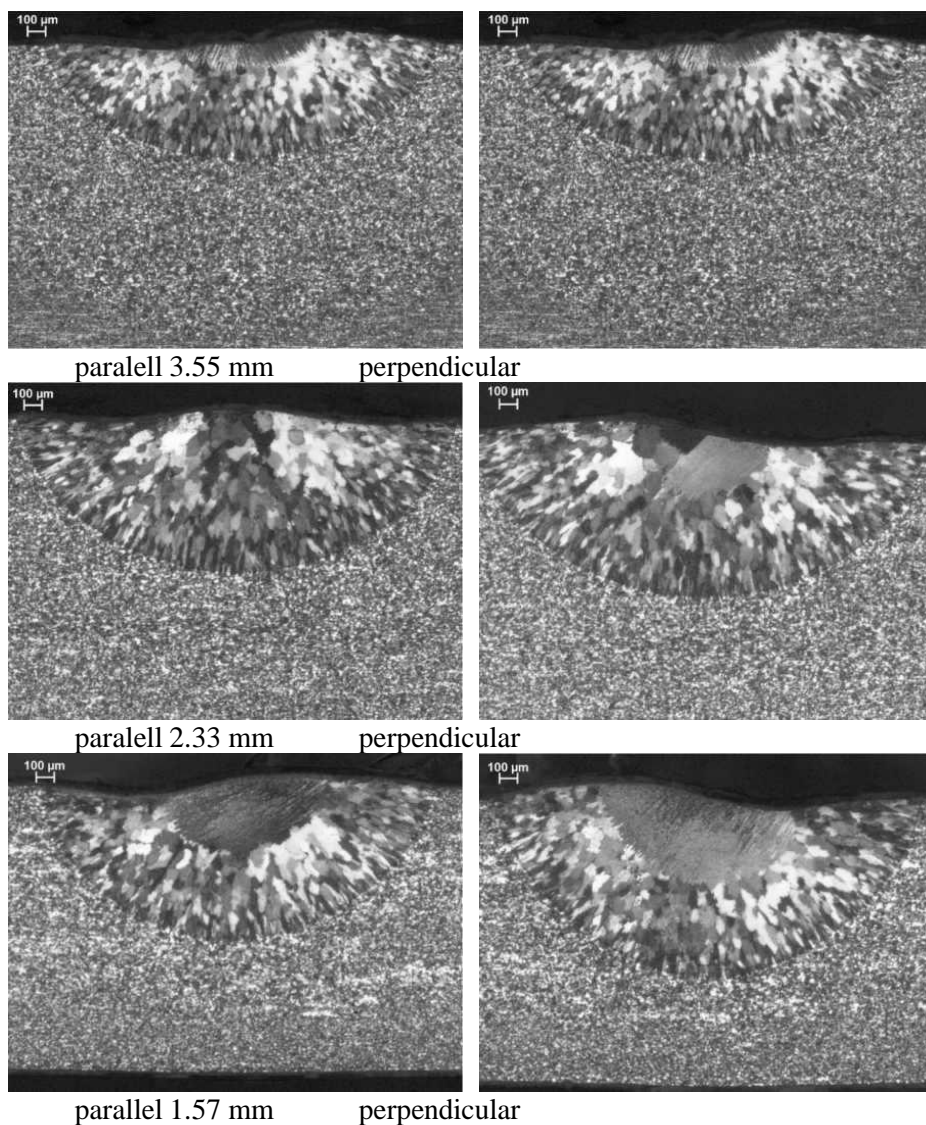

paralell 3.55 mm   perpendicular

paralell 2.33 mm   perpendicular

parallel 1.57 mm   perpendicular

Figure 2
The microstructures of LASER treated EN AW 8006 sheets

The extent of the heat affected zones is not visible on these images, so mosaic images also were made, where the whole cross section of the examined sample was visible. *Figure 4* shows the mosaic images taken from the thinnest sheets. The heat affected zone so large that whole cross section was recrystallized in one and a half distance as the molten pool. But the applied LASER power in this case was the smallest.
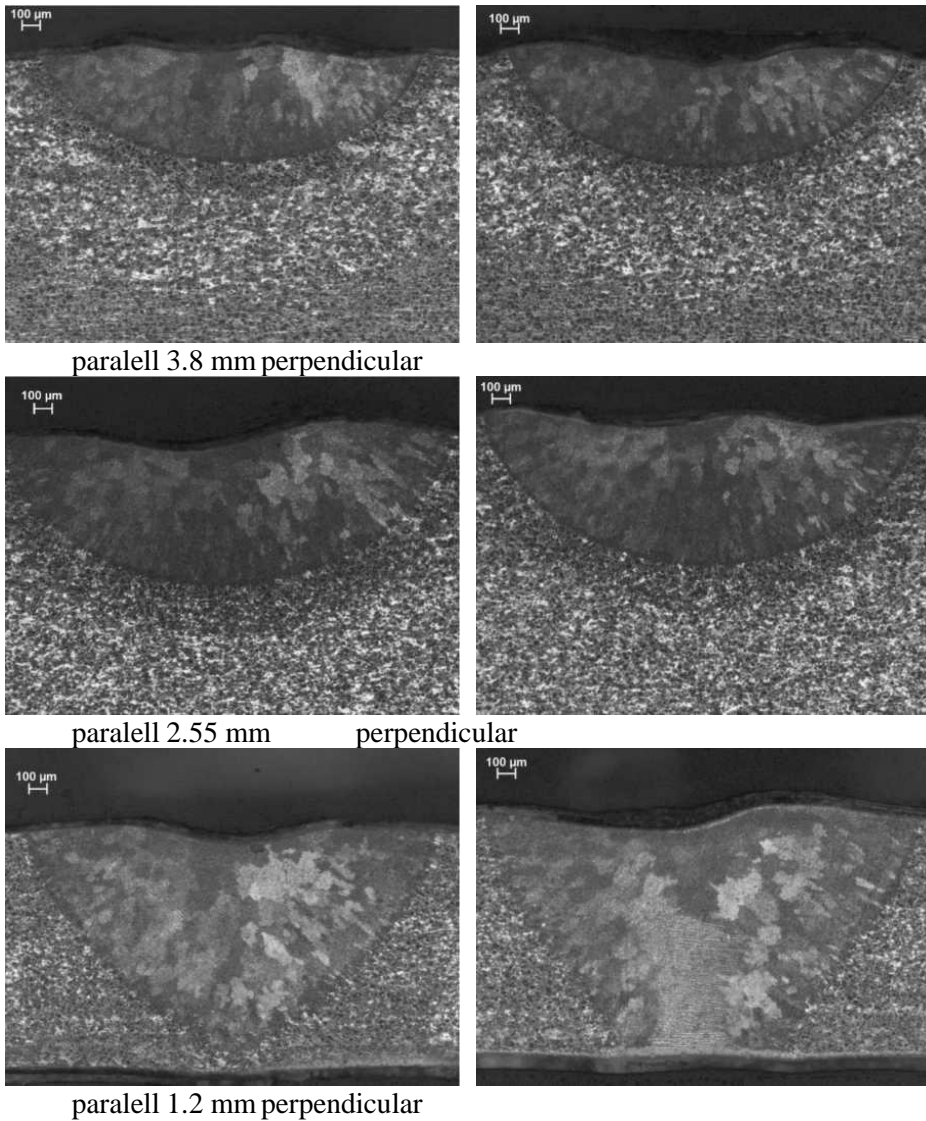

paralell 3.8 mm perpendicular

paralell 2.55 mm   perpendicular

paralell 1.2 mm perpendicular

Figure 3
The microstructures of LASER treated Al1.4Si sheets

The heat affected zone at the smallest extent of deformation is quite small *(Figure 5)* but the applied LASER power in these cases was the largest. At his samples the sandwich like structures is observable. This means that the microstructure is differs at the surface area and the middle of the cross section. This structure is originated to the hot-rolling. In that cases where the extent and rate of hot rolling was not proper in the whole rolling this structure forms in the hot rolled sheets. After cold reductions this difference in cross section remains. Probably this is not only a difference in the microstructure but in the stored energy too.
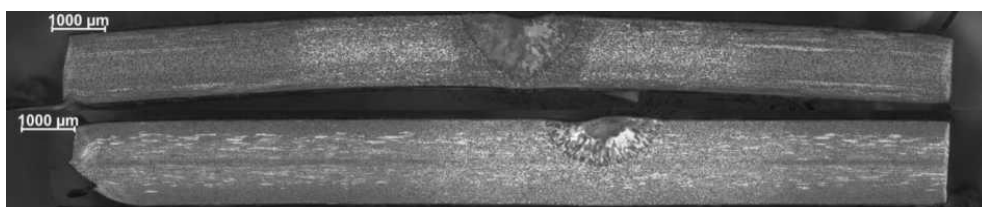

Figure 4
*The mosaic images of the microstructure of Al1.4Si 1.2 mm (up) and
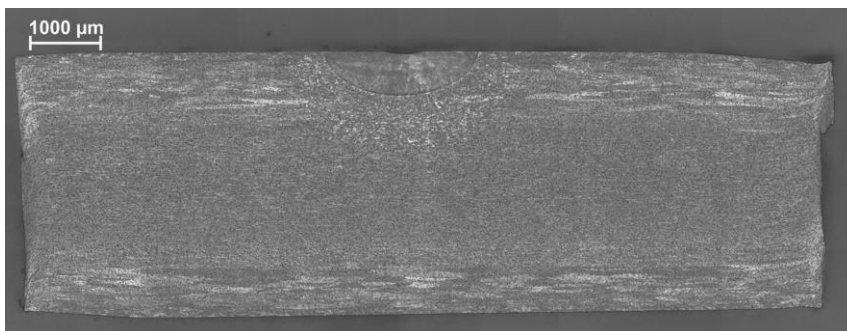EN AW 8006 1.57 mm (down) sheets*

Figure 5
The mosaic image of the microstructure of Al1.4Si 3.8 mm sheet
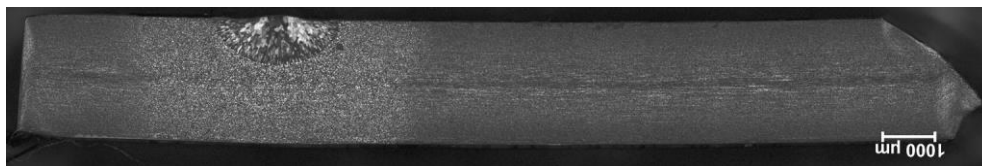

Figure 6
The mosaic image of the EN AW 8006 2.3 mm sheet

In the heat affected zone this difference does not cause any changes because of the extreme large heating rate and temperature. But this sandwich like structure cannot visible on the single micrographs.

The best result was achieved at the middle thickness where the applied LASER power was 900 W. The depth of the molten pool is nearly the quarter of the sheet thickness, but the extent of heat affected zone covers the whole cross section at the three times distance as the size of the pool. This is true at both alloys. There is a visible difference between the treatments parallel and perpendicular to the rolling direction. The molten pool is larger in case of perpendicular treatment. This difference become smaller with the increasing thickness due to the larger conducted heat.

CONCLUSION

EN AW 8006 and Al1.4Si cold rolled sheets annealed by LASER beam. The treatment performed parallel and perpendicular to the rolling direction of the sheets. Sheets with different extent of deformation were treated. The LASER power was adjusted to the sheet thickness. Thinner sheets were treated smaller power. The microstructure of the cross section of the sheets were compared. In all cases the sheets are partially molten. The molten volume was the largest at the thinnest sheets due to the small amount of conducted heat. In this case there are the largest difference between the parallel and perpendicular treatment. The size of the pool was larger in the case of perpendicular treatment. At wide sheets, where the LASER power was the largest the pool and the heat affected zone was the smallest. This was so small, that do not cover the whole cross section. The best results were achieved with the medium size sheets, where the pool was enough small, but the heat affected zone was enough large to modify the local properties of the sheet in advance. The grain size in the heat affected zone was extreme fine due to the large heating rate and temperature. Inhomogeneous Sandwich structure was observed in both alloys. This structure is originating to the not proper hot-rolling process. The inhomogeneous microstructure of the cold rolled sheets hasn't got a significant effect to the heat affected zone due to the mentioned large heating rate and temperature.

ACKNOWLEDGEMENT

REFERENCES

[1]   Bubonyi, T., Bánóczy, Zs., Barkóczy, P., Buza, G. (2018). Local Annealing of Aluminum Sheets by LASER Treatment. *Proceedings of the 6ᵗʰ*

International Scientific Conference of Advances in Mechanical Engineering (ISCAME 2018), Debrecen, pp. 29–30.

[2]   Borowski, J. & Bartkowiak K. (2010). Investigation of the influence of laser treatment parameters on the properties of the surface layer of aluminum alloys. *Physics Procedia*, vol. 5, pp. 449–456.

[3]   Fribourg, G., Deschamps, A., Bréchet, Y., Labeas, G., Heckenberger, U., Perez, M. (2011). Microstructure modifications induced by a laser surface treatment in an AA7449 aluminium alloy. *Materials Science and Engineering A*, vol. 528, pp. 2736–2747.

[4]   Chi, Y., Gu, G., Yu, H., Chen, C. (2018). Laser surface alloying on aluminum and its alloys: A review. *Optics and Lasers in Engineering*, vol. 100, pp. 23–37.

[5]   Singh, S. B. & Bhadeshia, H. K. D. H. (1998). Topology of grain deformation. *Material Science and Technology*, vol. 14, pp. 832–841.

[6]   Mandal, D. & Baker, I. (1995). Determination of the stored energy and recrystallization temperature as a function of depth after rolling of polycrystalline copper. *Scripta Metallurgica*, vol. 33, no. 4, pp. 645–650.

[7]   Hegyes, T. & Barkóczy, P. (2013). The Effect of Homogenization on the Annealing of Al-1.5%Mn Aluminum Alloy. *Materials Science Forum*, vol. 752, pp. 3–9.

[8]   Porter, D. A. & Easterling, K. E. (1996). *Phase Transformation in Metals and Alloys.* London: Chapman & Hall.

[9]   Cotterill, P. & Mould, P. R. (1982). *Recrystallization and Grain Growth in Metals.* London: Surrey University Press.

[10]   Barkóczy, P., Buza, G., Gyöngyösi, Sz. (2010). Lokálisan lágyított alumínium ötvözetek mikroszerkezetének vizsgálata. *XXIV. Hőkezelő és anyagtudomány a gépgyártásban országos konferencia és szakkiállítás*, Balatonfüred.

[11]   Bernolák, K. (1981). *A Fény*. Budapest: Műszaki Könyvkiadó.

[12]   Totten, G. E. & MacKenzie, S. (2003). *Handbook of Aluminum.* CRC Press.

PREPARATION OF GEOPOLYMER FOAMS USING AUTOCLAVE CURING

RÓBERT GÉBER[1]–ROLAND SZABÓ[2]–ISTVÁN KOCSERHA[3]

Geopolymers are potential substitute materials of traditional building materials. Geopolymer foams are also perspective materials for different foamed construction materials, like autoclave aerated concretes. In this research geopolymer foams (GPF) were prepared using fly ash, sodium-hydroxide alkaline activator and aluminum paste as foaming agent. Different curing conditions (curing in furnace and curing in autoclave) were applied on the samples. Density and compressive strength were determined, SEM and FTIR tests were done on GPFs, as well. The results show that compressive strength is highly affected by the pore forming mechanisms, which influencing the porosity of GPF, however the autoclave curing has less impact on the strength.

Keywords: autoclave, compressive strength, foam, FTIR, geopolymer

INTRODUCTION

Geopolymers are artificial materials, which can be an alternative for substituting conventional concrete [1]. These materials are inorganic polymer-structured binders. As source materials different aluminosilicate materials are used. For the geopolymerization reaction alkali activator is required, which is mixed together with raw materials. During the mixing process exothermic reaction is occur, then a so-called "artificial stone" is formed [2], [3]. As solid source different waste materials, by-products (e.g. cuttings, brick powder, fly ash, red mud, concrete powder, blast furnace slag) and natural sources (e.g. metakaolin) can be used, as well [4], [5], [6]. There are beneficial properties of these materials: fire and heat resistance, excellent mechanical strength, low shrinkage, excellent immobilising capability of heavy metals [1].

Like concrete, geopolymers can be foamed, as well. In order to prepare low density, high porosity foamed materials, aluminum powder (or paste), or hydrogen-peroxide are generally used [7], [8], [9], [10], [11], [12], [13], [14], [15].

[1]   Institute of Ceramics and Polymer Engineering, University of Miskolc
       H-3515 Miskolc-Egyetemváros, Hungary
       robert.geber@uni-miskolc.hu
[2]   Institute of Raw Material Preparation and Environmental Processing, University of Miskolc
       H-3515 Miskolc-Egyetemváros, Hungary
       ejtszabor@uni-miskolc.hu
[3]   Institute of Ceramics and Polymer Engineering, University of Miskolc
       H-3515 Miskolc-Egyetemváros, Hungary
       istvan.kocserha@uni-miskolc.hu

Researches are mainly focusing on the usability of different secondary raw materials and industrial wastes (for example incinerator bottom ash, ground granulated blast furnace slag, recycled aluminum foil) as geopolymer raw materials [16], [17], [18], [19], [20] and curing conditions. However, there are only a few researches dealt with autoclave cured foamed geopolymers. *Table 1* summarizes the main results of these researches.

Table 1

Curing method, conditions and some results of autoclaved geopolymers

Ref.	Curing method	Curing conditions	Result of curing
[21]	Dry autoclave curing	Day 1: T = 80 °C, p = 0.2 MPa Day 2: T = 80 °C, p = 0.2 MPa Day 3: drying at 80 °C	bulk density decreased; water absorption increased; compressive strength decreased
[22]	Autoclave curing	T = 150 °C; p = 2 MPa; curing time: 3 hours	compressive strength increased
[23]	Autoclave curing	T = 80–120 °C; p = 0.1 MPa; curing time: 4–48 hours	density of geopolymer can be achieve: 1,000–1,700 kg/m^3
[24]	Autoclave curing	T = 150 °C; curing time: 2 hours	increase in compressive strength
[25]	Climatic chamber or furnace or autoclave can be used for harden the geopolymer at higher temperatures.	$T_{min} = 40$ °C	curing time of geopolymer is shorter
[26]	Heating chamber or hot air oven or autoclave	T = 80 °C; p = 2.05 MPa; curing time: 1–24 hours	increase in compressive strength; decrease in thermal conductivity

This study focuses on the autoclave curing in order to improve the properties of geopolymer foams.

1. MATERIALS AND METHODS

1.1. Sample preparation

Geopolymer foams (GPF) were prepared using Class F type fly ash and sodium-hydroxide (NaOH) alkaline activator. Fly ash was first dried before mixing after that it was mixed with alkaline activator. Finally, aluminum paste (as a foaming agent) was added to the mix. Standard mixing time was used until homogenous mortar was obtained. After mixing, samples were poured into cylindrical plastic moulds with a diameter of 55 mm and 100 mm of height. The samples were demoulded in the next day, then were placed 1) into furnace for 6 hours at 60 °C (reference samples) and 2) into autoclave for 6 hours at different temperatures and pressures.

1.2. Curing conditions

Geopolymer foam samples were cured using the following conditions according to *Table 2*.

Curing method	Curing conditions		
Curing in furnace	60 °C		
Curing in autoclave	2 bar/60 °C	2 bar/75 °C	2 bar/90 °C
	4 bar/60 °C	4 bar/75 °C	4 bar/90 °C
	7 bar/60 °C	7 bar/75 °C	7 bar/90 °C

In order to compare the influence of curing in furnace with autoclave, curing time in furnace and in autoclave was set to 6 hours. The required temperature was reached in the autoclave in 2 hours after that 4 hours of dwell time was applied. At the end of curing passive cooling was used to reach room temperature.

1.3. Testing methods

Fourier-transformation infrared spectroscopy (FTIR) was applied to determine organic components within the samples. FTIR analysis is an appropriate method to study the structural evolution of amorphous alumino-silicates. Infrared absorption bands enable the identification of structures and specific molecular components, as well. Bruker Tensor 27 equipped with ATR cell was used to measure the absorbance of powdered GPF samples. Background spectrum was measured at every single run. The resolution was 4 cm^{-1}, sample scan time was set to 64 in the measuring range of 4000 cm^{-1} – 500 cm^{-1}. To observe the microstructure and cell structure of GPF samples scanning electronmicroscopy was used (Hitachi TM-1000). Electronmicrographs were taken in different magnifications. Uniaxial compressive strength tests were done on GPF samples. Instron 5566 type universal testing machine were used for mechanical tests. Cylindrical samples were tested using 5 mm/min rate compression.

2. RESULTS AND DISCUSSION

2.1. Microstructure of geopolymer foams

Figure 1 shows the microstructure of geopolymer foams cured at different methods. The SEM micrographs show the surface characteristics of extremas (reference samples cured in furnace; other samples cured in autoclave at 7 bars, 90 °C). In both cases large cavities/cells can be shown, which were generated by the evolved H_2 gas from the reaction of Al paste and water. The sizes of cells are varied from 50 μm to 1 mm and the distribution of cells are inhomogeneous. Observing the microstructure at higher magnification, a matrix can be seen, which attributes to the geopolymer matrix. As it is shown, the structure of this matrix was changed by applying high pressure and temperature. This matrix is more coherent, in which not dissolved fly ash particles are taken place. It refers to a strengthened geopolymer structure.
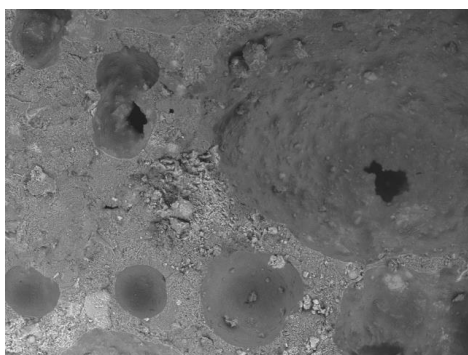
Cured in furnace at 60 °C (M = 200X)
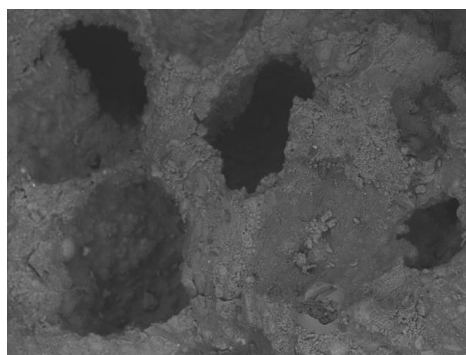
Cured in autoclave at 90 °C, 7 bar
(M = 250X)
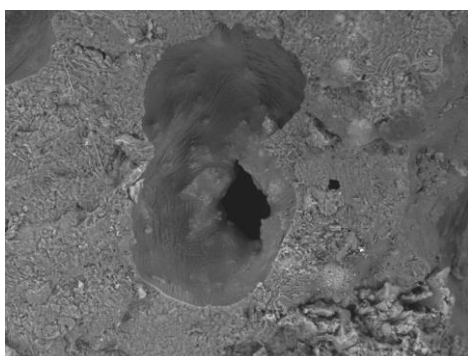
Cured in furnace at 60 °C (M = 500X)
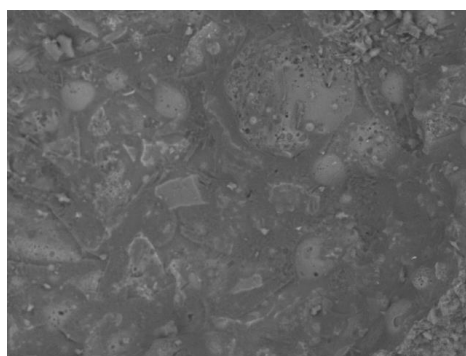
Cured in autoclave at 90 °C, 7 bar
(M = 1000X)
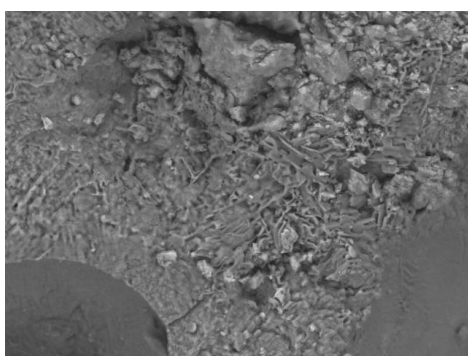
Cured in furnace at 60 °C
(M = 1000X)
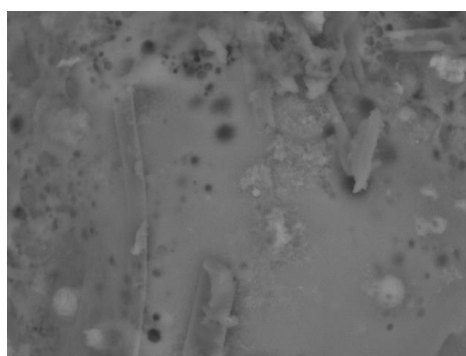
Cured in autoclave at 90 °C, 7 bar
(M = 5000X)

Figure 1
SEM micrographs of GPF samples cured at different conditions

2.2. Fourier transformation infrared spectroscopy

As an example *Figure 2* shows the FTIR spectras of geopolymer foams cured in furnace and in autoclave at 7 bars. *Table 3* contains the characteristic FTIR bands of the prepared geopolymer foams.
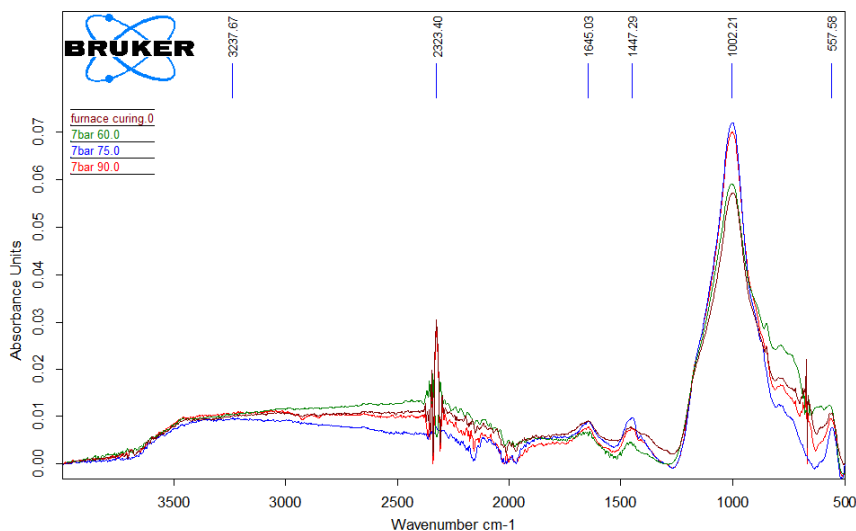
Figure 2

FTIR spectras of GPF samples cured at different temperatures and 7 bar pressure

Table 3

Characteristic FTIR bands of geopolymer foams

Peak position [cm^{-1}]	Assignment
3,050–3,240	Stretching vibration (–OH, H–OH)
1,640–1,645	Asymmetric bending vibration (H–OH)
1,445–1,460	Stretching vibration (O–C–O)
995–1,005	Asymmetric stretching vibration (T–O–Si, T=Si or Al)
850	Si-O stretching, OH bending (Si–OH)
775–790	Symmetric stretching vibration (Si–O–Si)
664–677	Symmetric stretching vibration (Si–O–Si and Al–O–Al)
557–566	Symmetric stretching vibration (Si–O–Si and Al–O–Al)

According to *Table 3* the following conclusion can be made. The peaks in the region of 3,050–3,240 cm^{-1} belong to the stretching vibrations of –OH and H–OH of bound water molecules, which are absorbed on the surface or entrapped in the large cells of the foam structure. The peaks in the region of 995–1,005 cm^{-1} are also confirm the

formation of geopolymer material. The main peak on the spectras are attributed to the Si–O stretching and OH bending vibrations and the asymmetric stretching vibrations of T–O–Si (whereas T means tetrahedrally bonded Si or Al). In the lowest region (557–790 cm^{-1}) the symmetric stretching vibrations of Si–O–Si and Al–O–Al are represented. In the range of 1,445–1,460 cm^{-1} the peaks attributed to the stretching vibrations of O–C–O. These peaks pointed out the presence of $NaHCO_3$, which can be formed during the carbonation of NaOH solution in air.

The effect of curing temperature and pressure on the structure of geopolymer foams can also observable. 2 bars and 4 bars of autoclaving pressure have not changed the structure of geopolymer foams. In these cases, the same peaks were detected with a little peak shifts, however, 7 bars of autoclaving pressure effected on the structure. In the range of 557–1,002 cm^{-1} no peaks were detected, which shows, that there were no symmetric stretching vibrations of Si–O–Si and Al–O–Al. Si–O stretching and OH bending vibrations were not detected, as well. Generally speaking, the higher the curing temperature the higher the intensity of peaks.

2.3. Density changes of geopolymers foams

As a foamed structure, density of geopolymer foams is an important property. As foamed materials are mainly used as a thermal insulator, it is important to reach a low density during production.

During the sample preparation the density of geopolymer foams were set to an average density of 0.5 g/cm^3. After curing in autoclave the dimensions and weight were measured on the samples in order to determine their density. The average values are shown in *Figure 3*.
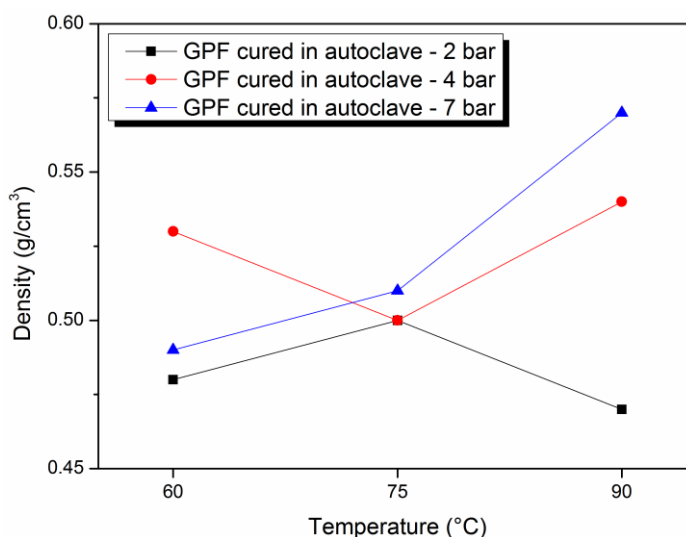
Figure 3
Density changes of geopolymer foams cured in autoclave

It can be concluded, that curing pressure and temperature have an effect on the density of GPFs. Using 2 bars of pressure the density curve has a local maximum point at T = 75 °C. Inversely, with the increase of pressure up to 4 bars a local minimum value can be shown at T = 75 °C, as well. 7 bars of autoclaving pressure unambiguously increasing the density. According to this, there was some kind of change within the GPF structure.

2.4. Compressive strength tests of geopolymer foams

As density, compressive strength is also an important material property of GPFs. *Figure 4* shows the results of uniaxial compressive strength tests.
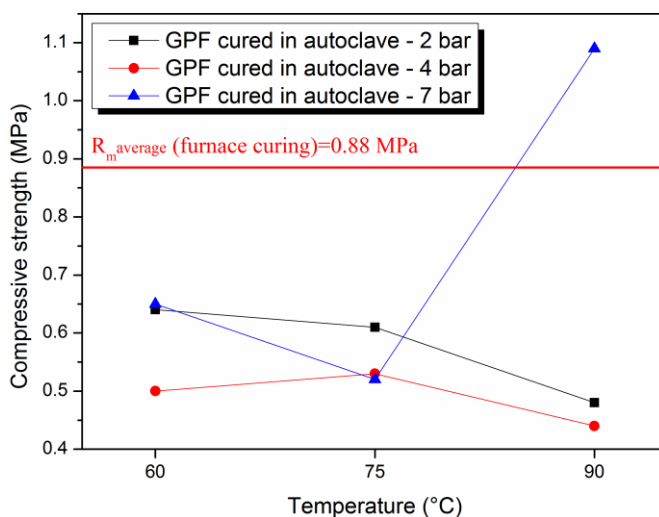
Figure 4
Compressive strength of geopolymer foams cured in autoclave

As it is shown in *Figure 4* increasing the curing temperature up to 75 °C only the samples cured at 4 bar were slightly increased. The highest curing temperature resulted more decrease in the compressive strength, however at 7 bars of pressure compressive strength was increased ($R_{m, 7\,bar, 90\,°C}$ = 1.09 MPa).

It can be concluded, that there is no clear correlation between compressive strength and density of samples cured in autoclave. Only at 90 °C and 7 bars of pressure in the autoclave shows some correlation. The reason of this could be the coherent geopolymer matrix, which were above mentioned.

CONCLUSION

The aim of this research was to study the effect of autoclaving curing on the properties of geopolymer foams. According to the results the following conclusion can be made:

- The structure of the geopolymer matrix was changed by applying high pressure (7 bars) and temperature (90 °C). These curing conditions resulted a strengthened geopolymer structure. These changes cannot be observed at lower temperatures and pressures.
- 7 bars of autoclaving pressure effected on the structure of geopolymer foams. FTIR test results confirm, that in the range of 557–1,002 cm^{-1} there were no peaks detected, therefore structural changes occurred.
- The highest compressive strength was reached at 7 bar at 90 °C, however autoclaving effects less on the compressive strength.
- Overall it can be said, that using autoclave for curing geopolymer foams, structural changes can be reach only at high pressure and high temperature.

REFERENCES

[1] De Weerdt, K. (2011). *Geopolymers – State of the art*. COIN Project report 37.

[2] Lin, H., Koumoto, K., Kriven, W. M., Garcia, E., Reimanis, I. E., Norton, D. P. (eds.) (2009). *Developments in strategic materials. A Collection of Papers Presented at the 32nd lnternational Conference on Advanced Ceramics and Composites* January 27–February 7. Daytona Beach, Florida: Wiley.

[3] Mucsi G., Csőke B., Molnár Z. (2012). Alkáli aktivált pernyealapú kötőanyag vizsgálata. *Hulladék Online*, vol. 3, no. 1, pp. 1–11.

[4] Mucsi, G., Molnár, Z., Kumar, S. (2014). Geopolymerisation of Mechanically Activated Lignite and Brown Coal Fly Ash. *Acta Physica Polonica, A.,* vol. 126, no. 4, pp. 994–998.

[5] Mucsi, G., Szabó, R., Rácz, Á., Kristály, F., Kumar, S. (2019). Combined utilization of red mud and mechanically activated fly ash in geopolymer. *Rudarsko-Geolosko-Naftni Zbornik,* vol. 34, no. 1, pp. 27-36.

[6] Mucsi, G. Szenczi, Á., Molnár, Z., Lakatos, J. (2016). Structural formation and leaching behavior of mechanically activated lignite fly ash based geopolymer. *Journal of Environmental Engineering and Landscape Management,* vol. 24, no. 1, pp. 48–59.

[7] Bai, C., Ni, T., Wang, Q., Li, H., Colombo, P. (2018). Porosity, mechanical and insulating properties of geopolymer foams using vegetable oil as the stabilizing agent. *Journal of the European Ceramic Society,* vol. 38, pp. 799–805.

[8] Zhang, Z., Provis, J. L., Reid, A., Wang, H. (2015). Mechanical, thermal insulation, thermal resistance and acoustic absorption properties of geopolymer foam concrete. *Cement & Concrete Composites,* vol. 62, pp. 97–105.

[9] Font, A., Borrachero, M. V., Soriano, L., Monzó, J., Payá, J. (2017). Geopolymer eco-cellular concrete (GECC) based on fluid catalytic cracking catalyst residue (FCC) with addition of recycled aluminium foil powder. *Journal of Cleaner Production*, vol. 168, pp. 1120–1131.

[10] Zhu, W., Rao, X. H., Liu, Y., Yang, E.-H. (2018). Lightweight aerated metakaolin-based geopolymer incorporating municipal solid waste incineration bottom ash as gas-forming agent. *Journal of Cleaner Production,* vol. 177, pp. 775–781.

[11] Chen, Z., Liu, Y., Zhu, W., Yang, E.-H. (2016). Incinerator bottom ash (IBA) aerated geopolymer. *Construction and Building Materials,* vol. 112, pp. 1025–1031.

[12] Aguilar, R. A., Burciaga Díaz, O., Escalante García, J. I. (2010). Lightweight concretes of activated metakaolin–fly ash binders, with blast furnace slag aggregates. *Construction and Building Materials,* vol. 24, pp. 1166–1175.

[13] Hlaváček, P., Šmilauer, V., Škvára, F., Kopecký, L., Šulz, R. (2015). Inorganic foams made from alkali-activated fly ash: Mechanical, chemicaland physical properties. *Journal of the European Ceramic Society,* vol. 35, pp. 703–709.

[14] Liu, M. Y. J., Alengaram, U. J., Jumaat, M. Z., Mo, K. H. (2014). Evaluation of thermal conductivity, mechanical and transportproperties of lightweight aggregate foamed geopolymer concrete. *Energy and Buildings,* vol. 72, pp. 238–245.

[15] Ducman, V., Korat, L. (2016). Characterization of geopolymer fly-ash based foams obtained with the addition of Al powder or H_2O_2 as foaming agents. *Materials Characterization,* vol. 113, pp. 207–213.

[16] Keulen, A., Kakebeeke, P. I. J. (2013). Geopolymer materials comprising alkaline activator and an additive selected from sugar and/or organic acids. *Patent WO2015076675A1*.

[17] Hao, H. C., Qin, Z. (2014). Preparation method of geopolymer-based fiberboard with red mud as raw material. *Patent CN103951332A*.

[18] Bondar, D., Lynsdale, C. J., Milestone, N. B., Hassani, N., Ramezanianpour, A. A. (2010). Geopolymer Cement from Alkali-Activated Natural Pozzolans: Effect of Addition of Minerals. *2nd International Conference on Sustainable Construction Materials and Technologies*.

[19] Narayanan, A. Shanmugasundaram, P. (2017). An Experimental Investigation on Fly ash-based Geopolymer Mortar under different curing regime for Thermal Analysis. *Energy and Buildings*, vol. 138, pp. 539–545.

[20] Yunsheng, Z., Wei, S., Qianli, C., Lin, C. (2007). Synthesis and heavy metal immobilization behaviors of slag based geopolymer. *Journal of Hazardous Materials,* vol. 143, pp. 206–213.

[21] Hanayneh, B. (2014). Influence of Curing Conditions on the Properties of Geopolymers from Untreated Kaolinite. *Journal of American Science,* vol. 10, no. 3. pp. 42–49.

[22] Bondar, D., Lynsdale, C. J., Milestone, N. B., Hassani, N., Ramezanianpour, A. A. (2010). Geopolymer Cement from Alkali-Activated Natural Pozzolans: Effect of Addition of Minerals. *2ⁿᵈ International Conference on Sustainable Construction Materials and Technologies*.

[23] Hao, H. C., Qin, Z. (2014). Preparation method of geopolymer-based fiberboard with red mud as raw material. *Patent CN103951332A*.

[24] Yunsheng, Z., Wei, S., Qianli, C., Lin, C. (2007). Synthesis and heavy metal immobilization behaviors of slag based geopolymer. *Journal of Hazardous Materials,* vol. 143, pp. 206–213.

[25] Keulen, A., Kakebeeke, P. I. J. (2013). Geopolymer materials comprising alkaline activator and an additive selected from sugar and/or organic acids. *Patent WO2015076675A1*.

[26] Narayanan, A. & Shanmugasundaram, P. (2017). An Experimental Investigation on Fly ash-based Geopolymer Mortar under different curing regime for Thermal Analysis. *Energy and Buildings*, vol. 138, pp. 539–545.

SURFACE PHENOMENA AND THE RESULTS
OF CHEMICAL ANALYSIS OF BRONZE ARTEFACTS

SZILVIA GYÖNGYÖSI[1]–LAURA JUHÁSZ[2]–
PÉTER BARKÓCZY[3]–JULIANNA CSEH[4]

The preferred method in natural scientific examination of Bronze-Age metallic artefacts is non-destructive surface analysis. One of the scopes of this type of investigations is the chemical analysis of the alloys. But the chemical composition of the surface is modified by surface phenomena such as micro- and macro-segregations or corrosion. The chemical analysis alone can show a different picture about the metal. This study collects and introduces some examples from a detailed research where the metallography of the objects shows different results and reveals the origin of the differences in bulk and surface analysis.

Keywords: metallography, artefacts, chemical analysis, surface, bronze

INTRODUCTION

Segregation phenomena take place in metals during the processing, mainly at crystallization and corrosion processes [1], [2]. Both processes have a great effect on the microstructure and chemical composition of artefacts from Bronze Age [3]. This early stage of metallurgy and processing technology could produce inhomogeneous materials [4]. The long-term corrosion processes have a great effect on the surface of the artefacts [5]. Therefore, every time the method of examination is a great question. The metallographic observations and descriptions provide the detailed information about the objects related to the microstructure and chemical composition [6]. Based on this data it is possible to describe the most probable production method. Some information could be uncovered on the smelting of ores and alloying by the analysis of inclusions and composition. Through the detailed testing of the corrosion layer, additional information appears from the utilization of the objects or the burial

---

[1]   Department of Solid State Physics, University of Debrecen
       H-4026 Debrecen, Bem Square 18, Hungary
       szilvia.gyongysi@science.unideb.hu

[2]   Department of Solid State Physics, University of Debrecen
       H-4026 Debrecen, Bem Square 18, Hungary
       laura.juhasz@science.unideb.hu

[3]   Department of Physical Metallurgy, Metalforming and Nanotechnology, University of Miskolc
       H-3515 Miskolc-Egyetemváros, Hungary
       fembarki@uni-miskolc.hu

[4]   Museum of Tatabánya
       H-2800 Tatabánya, Szent Borbála Square 1, Hungary
       juci.cseh@gmail.com

customs [7]. The metallography of Bronze Age objects gives detailed data and a lot of estimation could be made to excess the archeologic research based on them [8]. The only problem with metallography is that it is a destructive material testing method, so the sampling of the objects is necessary. Additionally, to obtain the largest amount of data the position of the sample is determined by the assumed processing technique. The function, the shape and sometimes the surface defects show the possible sequence of production steps [9]. Generally, the position of the samples needs a large area to be destructed [10]. When the principles of heritage protection are required to be taken into consideration, taking these kinds of samples is not allowed. Sampling can also be prohibited in cases of special or unique objects.

Modern analytical methods give the possibility to analyze the surface region without sampling or without destructing the objects. Therefore, this method is currently preferred by the archaeometric studies. Based on these studies average composition is defined, and using this as the raw material composition, hierarchical data clustering and analysis is performed. Another way to research the origin of the material is the Sn or Pb isotope analysis and clustering [11]. The data from these studies are sometimes confusing. Szabó [12] made a collection of analyzed data and shows that the tin content of the Bronze Age artefacts is dramatically increasing when the analyzed volume is decreased. These tests are made at the surface or close to the surface and Szabó clearly shows that the cause of this phenomena is tin segregation at the surface. Szabó estimates there are some technological specialties where this can be reached artificially, however as presented in this study, the corrosion processes are enough to cause it.

Another problem with these techniques and methods is that generally only the chemical composition is revealed without any information on the microstructure. The smelting, alloying and processing has a strong effect to the microstructure of the forming phases. Without analyzing the phases, estimating the chemical composition of the raw material, in this case the copper, is impossible. The local chemical analysis is just a part of the necessary information. Due to heritage protection usually this is the only possibility, but in this case, it is necessary to take this into consideration during the interpretation of the data.

This study introduces this problem through the analysis of three objects from the cemetery of Vértesszőlős, excavated and studied by Julianna Cseh – Museum of Tatabanya.

Metallographic sample was prepared from one object. This object is unique, but it has great importance from an archeologic point of view. Therefore, the interest overwrites the heritage protection. The samples were taken from a part of the objects in a way that allows the full restoration of the objects. Sampling of other samples was prohibited. In case of one sample it was possible to remove enough material to study the composition of the bulk material and the surface together. The third sample was examined with minimal preparation. The chemical composition of the samples is compared in this article.

1. MATERIALS AND METHODS

Three different artefacts from Vértesszőlős cemetery were chosen: an anthropomorphic pendant, a wheel-like pendant and a disc headed pin. All of them are bronze artefacts. A sample was taken from the anthropomorphic pendant for metallographic examination. The cut surface of the sample was grinded and polished mechanically, than immersion etching was made using a K_2CrO_4 and water solution. The sample was examined by OM and SEM-EDS technique. Sampling of the wheel and the pin was not allowed. A small surface area was grinded on both artefacts. The grinding was made deep enough to reach the metallic material. This area was examined by SEM-EDS. The local chemical composition was measured and compared after the different sample preparation. A Zeiss AxioImager optical- and a Hitachi S4300 CFE electron microscope was used for the observation and analysis.

2. RESULTS AND DISCUSSION

Figure 1 shows the position of the sample taken from the anthropomorphic pendant and it's a low magnification optical micrograph. The estimated production technique is casting and free hammering. Therefore, the largest area of the shape was chosen for sampling where the effect of the hammering can be observed clearly. At first sight a large corrosion layer can be observed. The thickness of the layer is ~0.5 mm. A smooth transition zone was found between the corrosion layer and the bulk metal. At larger magnification *(Figure 2)* a recrystallized microstructure appears with small grains. This suggests a heating after cold hammering, which is a typical technological method in this period. At higher magnification the composition difference caused by the microsegregation during crystallization shows the original dendritic structure, and within this structure the small recrystallized grains can be seen. Only a small extent of cold hammering is assumed based on this. Additionally, this explain the nature of the transition zone. The corrosion process was faster in the segregated zones between the dendrite arms. The hammering makes the direction of the dendrites perpendicular to the direction of hammering, so an elongated nature of the transition zone also can be seen.

When visual examination shows metallic a surface, the measured composition is the combination of the original composition of the metal and the corrosion layer. For the accurate measurement the corrosion layer must be removed at 0.5 mm depth. This destruction is comparable to sampling.

The chemical composition of the metal is measured in ACS1 area. The tin content is 9.1 w/w%, which is normal in that case when the casting plays a significant role in the production. This composition is near to the limit where the tin bronze can plastically deform. Next to the tin a small amount of Sulphur (0.31 w/w%) and phosphorus (0.24 w/w%) content was measured which is originated to the smelting process. 0.81 w/w% silver content can also be detected. Recently the assumed source of silver is the copper ore.
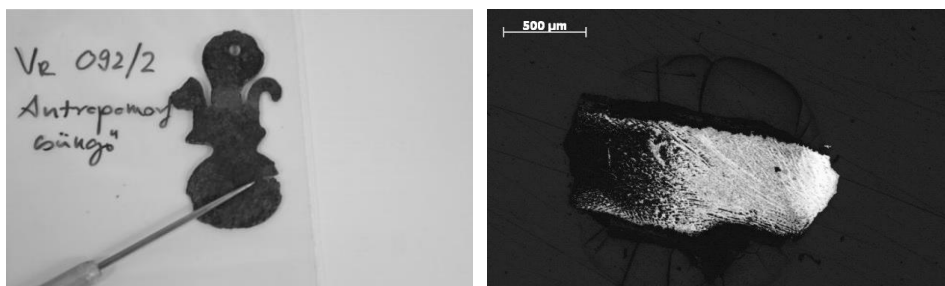
Figure 1
*The position and the prepared surface of the metallographic sample are taken
from the anthropomorphic pendant*
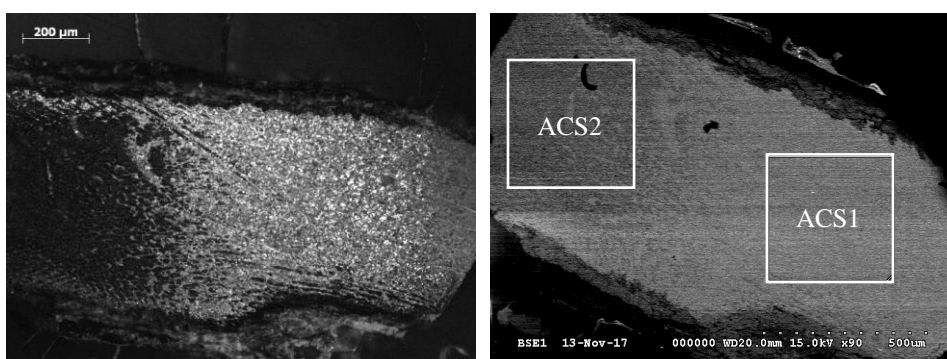
Figure 2
*Optical and SEM micrographs from the microstructure of antropomorhic pendant.
The areas of the local chemical analysis are signed of the SEM micrograph
by ACS1 and ACS2*
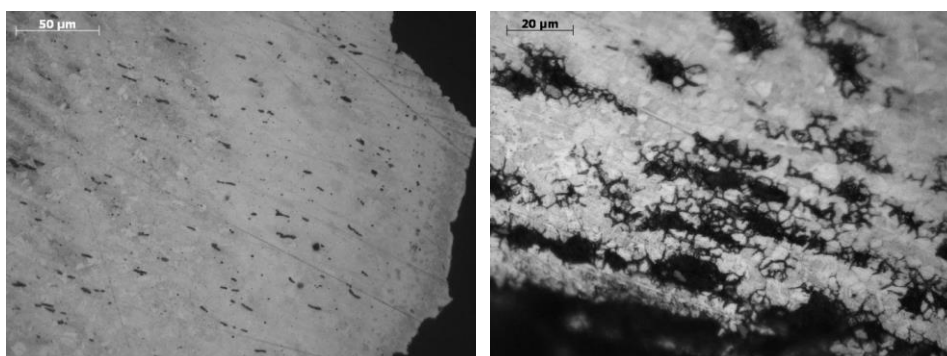
Figure 3
*The microstructure of the anthropomorphic pendant in lower and higher
magnification. The high magnification reveals the primary dendritic
structure driven corrosion process*

The chemical composition of the corrosion layer is measured at ACS2 area. The tin content here is nearly double (15.6 w/w%). The phosphorus disappeared from the layer; the Sulphur level is nearly the same (0.23 w/w%). The silver content increased also dramatically to 2.35 w/w%. Several elements were detected and measured which are not contained in the raw metal, these originate from to the soil: Mg, Al, Ti, Cr, Mn, Co. The main problem is that such elements are also measured in the corrosion layer which are used as an indicator of certain ore source. These are the Ni, Fe, Sb and As. All these elements are treated as trace, and within a small range classify the metals. But these metals are not detected in the raw metal. The surface and the bulk analysis can classify the origin to two totally different source, if the extremely high tin and silver content are not taken into consideration, because the microstructure cannot be revealed by a surface analytical method. So, the fact of hammering in this case is unknown, and the high tin content can suggest a casting process only.

In higher magnification due to the originally segregated metal, tin and silver particles can be seen in the corrosion layer. These metals segregate during the corrosion reactions in this nearly pure form. These particles are quite small ones (1–3 µm). But as Szabó showed, the examined volume with the development of the equipment is decreasing, therefore it is possible to measure extreme high tin and silver content in this case.

This comparison of the surface region and the bulk metal shows a lot of questions. Therefore, as a case study two other object were examined, but only at the surface of the artefacts. *Figure 4* show the wheel shaped pendant and the measurement set-up. More corrosion layer was removed by grinding while the bronze metal appears to see the previous study. Nearly a similar tin content was measured (8.3 w/w%). High As (2.2 w/w%) an Ni (1.1 w/w%) content was also detected. It is hard to decide if this is the real concentration, or the segregation increases the amount of these element.

Figure 4
The wheel-like pendant, and the measurement set-up at SEM chamber

The advantage of the SEM-EDS technique is that visual information also available. A map and a line analysis were made to study the distribution of the elements. The bright area shows the metal, the dark area is the corrosion product on the surface of the object. there is a grey transition zone where the thickness of the corrosion product is smaller due to the curved surface. The map clearly shows the segregated region of tin. The line scan proves that this area is the light grey band between the metal and the corrosion product. The average copper concentration is the same as it was measured in the first analysis. Considering the copper distribution, when the copper content drops, the tin and oxygen content increase combined, so tin-oxide is assumed to be present in the metallic surface. This indicates that deeper grinding would reveal the real bulk metallic material a composition.
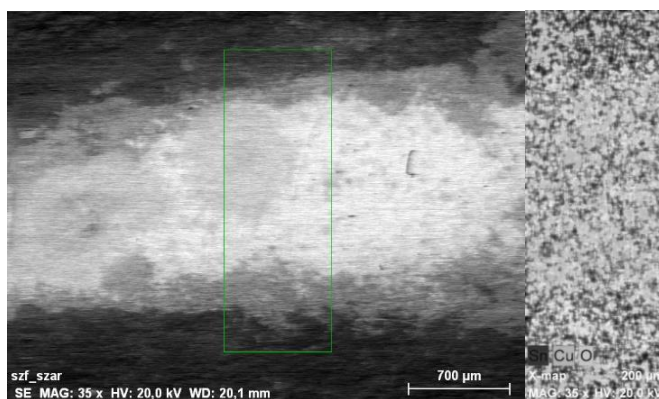

Figure 5
Local chemical analysis of wheel-like pendant by SEM-EDS, the right image shows the element map of the signed rectangle
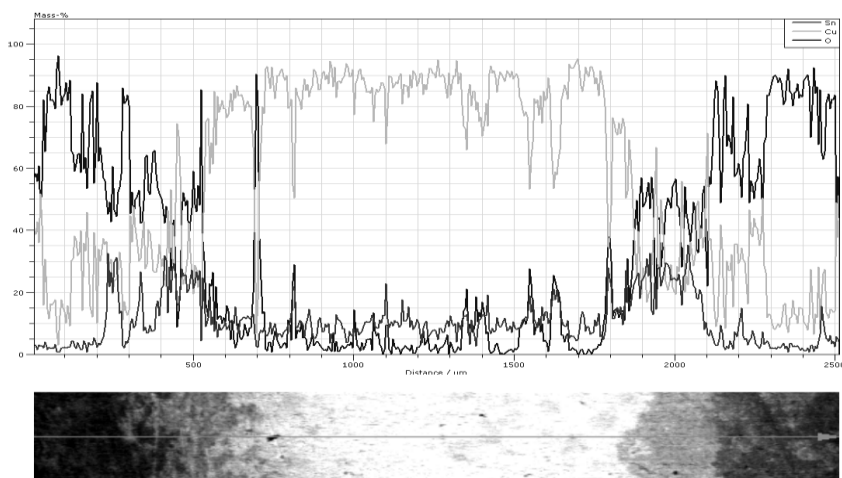

Figure 6
The element distribution along a line scan at the analysed area of wheel-like pendant

A disc headed pin was measured. These kinds of objects are rare, therefore the protection is the main issue in this case. Sampling was not allowed, so the surface was grinded cautiously, and just the necessary amount of material was removed until the bronze colour became visible. Then the composition of the object was measured by SEM-EDS *(Figure 7)*. Extremely high tin content was measured (27.1 w/w%). The colour of the alloy with such high tin content is white instead of the typical colour of bronze. Additionally, the alloy containing so much tin would be brittle, and it is impossible to deform plastically. Also, high arsenic (2.45 w/w%) and phosphorus (0.77 w/w%) content was measured. Iron (0.46 w/w%) and nickel (0.94 w/w%) were also detected. The origin of these metals cannot be identified in this case. These either can be contained from the metal or comes from the soil. The large aluminium (1.57 w/w%) and silicon (2.92 w/w%) content surely originates from the soil and the presence of these metals is due to the corrosion reactions. In this case the measured concentration is far from the original concentrations and does not show an acceptable picture about the object.

Figure 7
The position of the local chemical analysis of the disc headed pin and the set-up of the measurement

The current study uses EDS analysis, but the results are independent from the measuring technique, because the samples carry these composition differences themselves. This introduced problem with the concentration, and the question about the accuracy exists in all testing method where the sample was analysed from the surface region.

CONCLUSIONS

It is well known that the corrosion processes modify the concentration of the surface region in metallic materials. It is frequently true in the case of Bronze Age objects which went through a long-term corrosion and covered by a thick corrosion layer.

The segregation processes which takes place during the manufacturing processes also can modify the status, the structure and the thickness of the corrosion layers. Therefore, without measuring the real thickness of the corrosion layer, there is no chance to avoid the modification effects of the corrosion reactions, where some elements segregate and others disappear from the corrosion layer. If the measurement of the real metallic concentration is the aim, it is necessary to remove the whole corrosion layer when sampling is prohibited. In other cases, the metallographic analysis is the best way, where microstructural information also can be seen next to the local concentrations. In current researches the concentration of the metals is used in statistical analysis and comparisons to determine groups. In these cases, same elements are used as trace, which has small concentration. This study presented examples where the measurement in the surface layer can give a totally different picture about the metal. In that cases where the heritage protection allowed the metallography is the best way to analyze the metals and collect that information which helps the statistical analysis and the work of archeologists.

ACKNOWLEDGEMENT

REFERENCES

[1]   Davies, S. H. (2001). *Theory of Solidification*. Cambridge: Cambridge University Press.

[2]   Cramer, S. D., & Covino, B. S. Jr. (2005). *ASM Handbook 13: Corrosion*. ASM International.

[3]   Duberow, E., Pernicka, E., Krenn-Leeb, A. (2009). Eastern Alps or Western Carpathians: Early Bronze Age Metal within the Wieselburg Culture. In: Kienlin, T. L. & Roberts, B. (eds.): *Metals and Societies. Studies in honour of Barbara S. Ottaway.* Universitätsforschungen zur prähistorischen Archäologie 169. Bonn, 336–349.

[4]   Höppner, B., Bartelheim, M., Huijsmans, M., Krauss, R., Martinek, K. P., Pernicka, E., Schwab, E. (2005). Prehistoric copper production in the Inn Valley (Austria), and the earliest copper in Central Europe. *Archaeometry,* vol. 47, pp. 293–315.

[5]   Scott, D. A. (1991). *Metallography and Microstucture of Ancient and Historic Metals*. Singapore.

[6]   Török, B., Barkóczy, P., Kovács, Á. (2019). Miscrostruture analysis of metal artefacts from the Carpathian Basin: a brief methodology of the ARGUM's metallogrphy practice. *UISPP Journal*, vol. 2, no. 1, pp. 33–45.

[7]   Kiss, V., Fábián, Sz., Hajdu, T., Köhler, K., Kulcsár, G., Major, I., Serlegi, G., Szabó, G. (2016). From inhumation to cremation – changing burial rites in

Early and Middle Bronze Age Hungary. In: Kneisel, J., Nakoinz, O. (eds.): *Tipping point in the Bronze Age – Modes of change – inhumation versus cremation in Bronze Age burial rites*. International Open Workshop: Socio-Environmental Dynamics over the Last 12,000 Years: The Creation of Landscapes IV. Kiel.

[8] Hajdu, T., György-Toronyi, A., Pap, I., Rosendahl, W. (2016). The chronology and meaning of the Transdanubian encrusted pottery decoration. *Praehistorische Zeitschrift,* vol. 91, no. 2, pp. 353–368.

[9] Kienlin, T. L. (2013). Copper and Bronze: Bronze Age Metalworking in Context. In: Fokkens H. & Harding A. (eds.): *The Oxford Handbook of the European Bronze Age*. Oxford: Handbooks in Archaeology.

[10] Lutz, J., Pernicka, E. (1996). Energy dispersive X-ray analysis of ancient copper alloys: empirical values for precision and accuracy. *Archaeometry,* vol. 38, pp. 313–323.

[11] Nessel, B., Brügmann, G., Pernicka, E. (2019). Tin isotope ratios in early and middle Bronze Age bronzes from Central and Southeastern Europe. *UISPP Journal*, vol 2, no. 1, pp. 1–11.

[12] Szabó G. (2010). Az archeometallurgiai kutatások gyakorlati és etikai kérdései. Practical and ethical issues of archeometallurgic research. *Archeometriai Műhely*, vol. 2, pp. 111–122.

EFFECT OF TREATED ALUMINUM DROSS
ON THE PROPERTIES OF FOAMED CONCRETES

ALEXANDRA HAMZA[1]–ANDREA SIMON[2]

In this study, the effect of aluminum dross on the properties of concrete foams was investigated. Concrete was foamed by adding diluted (30 wt%) H_2O_2 solution. Before adding to the concrete, aluminum dross was water leached to remove fluxing salt residues. Ordinary Portland Cement (OPC) with a water/cement (w/c) ratio of 0.45 and 5 wt% dross was mixed to form slurry. Samples were cured in a humidity chamber for 28 days before the compressive strength tests. Bulk density, porosity and thermal conductivity of the foams were also investigated.

Keywords: dross, foam concrete, microstructure, strength, thermal conductivity

INTRODUCTION

Nowadays great attention is paid to improve the thermal insulation of building materials to meet the requirements of the increasingly strict energetic standards. One of the most widespread building material is concrete whose thermal conductivity can be reduced by the addition of various additives. Bulk density of load-bearing lightweight aggregate concretes ranges from 800 to 2,000 kg/m^3 (MSZ EN 4798:2016) [1]. The lightweight concrete of standard classification is shown in *Table 1*. In the production of lightweight aggregate concretes, low density additives (such as expanded clay, polystyrene, expanded perlite, etc.) are added to the slurry instead of the normal density additives [2].

Table 1
The range of body density tested according to MSZ EN 12390-7 [1]

The range of body density	D1.0	D1.2	D1.4	D1.6	D1.8	D2.0
kg/m^3	800–1,000	1,000–1,200	1,200–1,400	1,400–1,600	1,600–1,800	1,800–2,000

Lightweight concretes can be also made by increasing the porosity in the structure. Closed pores with a diameter of up to 2 mm can be produced by the addition of gas releasing or foaming additives. The latter is called foamed concrete, for which aluminum powder or H_2O_2 is used to produce [3]. Bulk density of foamed concretes used in

[1]   FIEK University of Miskolc
      H-3515 Miskolc-Egyetemváros, Hungary
      femhamza@uni-miskolc.hu

[2]   Institute of Ceramic and Polymer Engineering, University of Miskolc
      H-3515 Miskolc-Egyetemváros, Hungary
      femandi@uni-miskolc.hu

the building and construction industry generally ranges from 500–1,200 kg/m^3, with a thermal conductivity from 0.15–0.45 W/m·K and a compressive strength varying between 1.5–6.5 MPa [4]. When aluminum powder is used as a foaming agent, hydrogen gas is released by a chemical reaction in the alkaline medium of the slurry [5], [6]:

$$2\,Al + 2\,OH + 4\,H_2O \rightarrow 2\,AlO(OH)^{2-} + 3\,H_2 \tag{1}$$
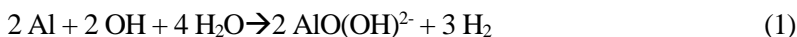
The pH of the alkaline medium should be about 12.5 [7,8]. The mechanism of action of the hydrogen peroxide is different, as H_2O_2 is known to be a strong oxidizing agent in which oxygen atoms are bonded to each other with a weak peroxo bond. Consequently, hydrogen peroxide is thermodynamically unstable and decomposes as follows:

$$2\,H_2O_2 = 2\,H_2O + O_2 \tag{2}$$

This decomposition process is used to foam cement and concrete. It is important to mention that cement foam is mostly produced without adding coarse grained sand. Hydrogen peroxide solution is stable at low pH, but decomposes at increasing alkalinity. Catalysts, such as Fe^{2+}, Cu^{2+}, Mn^{2+} and Co^{2+}, homolytically catalyze the decomposition [9]. As these metals are presented in every cement in different amounts, the foaming mechanism alternates with the type of commercial cements.

In this study, the effect of treated aluminum dross on the properties of foamed concrete was investigated. After that valuable metals have been extracted from the untreated dross, the residue can be reusable by applying a proper treatment [10], [11], [12]. As salts have a detrimental effect on construction and building materials, they have to be extracted from the dross [13]. Physical salt attack is a deterioration process caused by the crystallization of salts accumulated in the pores near to the evaporation surface of the concrete. The mechanism is called physical salt attack, because there is no chemical reaction between the concrete and the salt. Sodium sulfate, sodium carbonate and sodium chloride (in descending order of aggression) are among those salts which are responsible for the physical damage of concrete [14], [15], [16].

1. MATERIALS AND METHODS

1.1. Materials

For the research, Ordinary Portland Cement (OPC, CEM I 52.5 N) was used. This cement contains only clinker minerals and a small amount of gypsum that regulates the hardening rate. Mineral composition of the cement and drosses was measured by X-Ray Powder Diffraction with a Rigaku Miniflex II instrument applying Cu Kα radiation in the 2θ range from 3° to 90°. The main phases of the cement *(Figure 1)* are hatrurite [Ca$_3$(SiO$_4$)O], larnite [Ca$_2$SiO$_4$], portlandite [Ca(OH)$_2$], grossular [Ca$_3$Al$_2$(SiO$_4$)$_3$], brownmillerite [Ca$_2$(Al,Fe)$_2$O$_5$] and merwinite [Ca$_3$Mg(SiO$_4$)$_2$]. Drosses were treated with a hydrometallurgical process to remove metallic aluminum and fluxing salt residues. Drosses were water leached one (I), two (II) or three (III) times then ground to a particle size below 250 μm [17]. The composition of drosses did not change significantly by increasing the number of leachings. The main components *(Table 2)* are spinel

[MgO Al$_2$O$_3$], corundum [Al$_2$O$_3$] and wurtzit [AlN]. The total amount of salt residues varies between 1.6–2.6 wt%, which is not a significant amount.

SEM micrograph of the cement and treated drosses are shown in *Figure 2*. The cement powder shows a wide range of particle sizes having polyhedron shape. Dross particles have rough, irregular surface which becomes smoother with the number of leachings.

Table 2

Composition of drosses in wt% based on X-ray diffraction

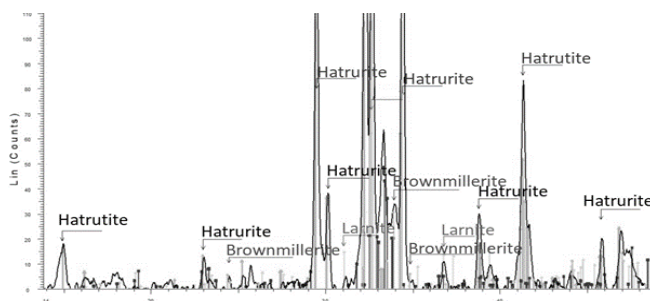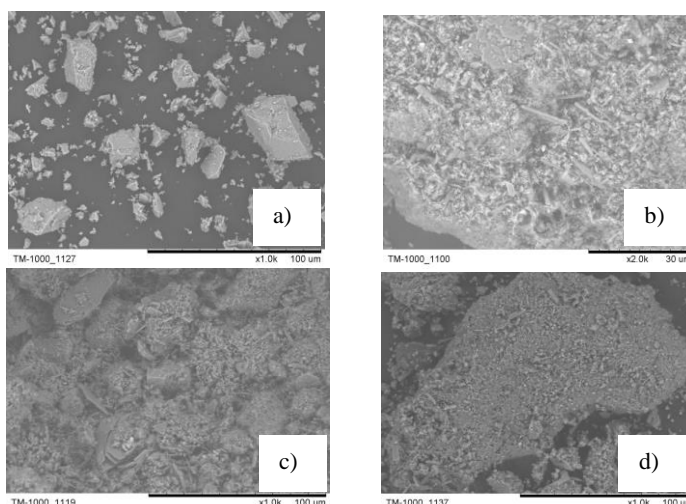| Dross	Al$_2$O$_3$	MgAl$_2$O$_4$	AlN	CaF$_2$	NaCl	KCl	Al(OH)$_3$	CaCO$_3$	MgO	Other	Total salt
I	22.20	53.46	19.25	0.83	1.41	0.18	–	2.08	0.59	Balance	2.43
II	21.54	53.71	17.66	0.70	1.50	0.39	1.40	2.40	0.09	Balance	2.56
III	20.38	52.82	17.35	0.81	0.66	0.10	3.88	2.92	0.61	Balance	1.57

Figure 1

XRD pattern of cement

Figure 2

SEM micrograph of a) cement b) Dross I c) Dross II d) Dross III

1.2. Methods

5 wt% dross – relative to the weight of the cement – was added to the cement. 70 ·70 ·70 mm molds were used to prepare samples for the compressive strength test. Prior to mixing, treated drosses were dried to constant weight in a laboratory chamber dryer. After drying, it was found that dross particles were agglomerated therefore it was necessary to crush them again using a porcelain mortar.

Dross and cement were manually dry mixed to homogeneous state. W/c (water/cement) ratio was 0.45 for each mixture. The composition of the mixtures is summarized in *Table 3*. After adding the appropriate amount of water, stirring was continued with an electric mixer until a homogeneous cement slurry was obtained. In the next step, diluted (30 wt%) H_2O_2 as foaming agent was added to the cement slurry at 4 wt% in relation to the weight of the cement. Incorporation of hydrogen peroxide was carried out by intense mechanical stirring. Foamed slurry was poured into molds coated previously with mold-releasing agent and then vibrated.

Table 3

The composition of the mixtures (I, II and III means the number of water leachings)

Materials	Reference	Dross I	Dross II	Dross III
Cement [g]	1,200	1,200	1,200	1,200
w/c ratio	0.45	0.45	0.45	0.45
Foaming agent [wt%]	4	4	4	4
Dross [wt%]	–	5	5	5
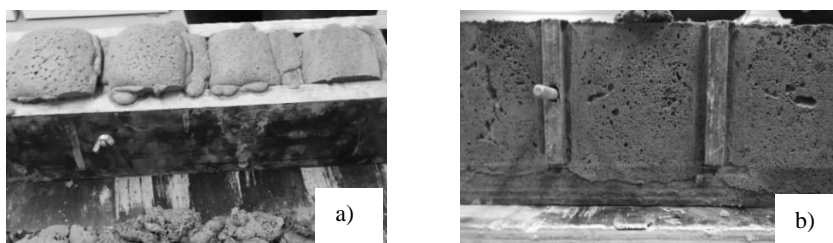
Figure 3
a) Foaming of the slurry b) Disassembly of molds

After that the foaming *(Figure 3a)* and hardening of the cement slurry had been finished, top of the samples were removed using a wire. After being kept in the mold for one more day, samples were removed *(Figure 3b)* and placed into a vapour chamber. The container was covered and samples had been cured for 28 days at 22 °C and 90% humidity.

Bulk density was calculated for three samples per mixtures. Samples were placed into the drying chamber after curing and dried to constant weight. After drying, lengths and weight of the cubes were measured and bulk density (kg/m^3) was calculated as mass per unit volume. Macrographs of the foamed samples were taken with a Canon EOS 700D camera. Pore size analysis was performed on macrographs of the foamed concretes using ImageJ free software. 10 measurements were averaged per sample.

Thermal conductivity was characterized by C-Therm TCi Thermal Conductivity Analyzer using Modified Transient Plane Source (MTPS) technique. During measurement, a known current is applied to the sensor that rises the temperature at the interface between the sensor and the sample resulting a change in the voltage drop of the sensor. The thermal conductivity is inversely proportional to the increment of the temperature. Six measurements were averaged for every mixture.

Compressive strength tests were performed on cured cube specimens at 28 days. 3 samples were tested and averaged per mixture. Fractured surfaces were observed with a Hitachi TM 1000 scanning electron microscope. In addition, the mineral composition of the 28-day samples was examined by X-Ray diffraction, as illustrated in *Figure 4*. The figure clearly shows that the formation of hydrate products is not influenced by the presence of the dross. The main components of the concrete foams are the phases originated from the hydration of the cement. Besides, the main phases of the dross (spinel, corundum and wurzite) are also found in small amount in samples containing dross.
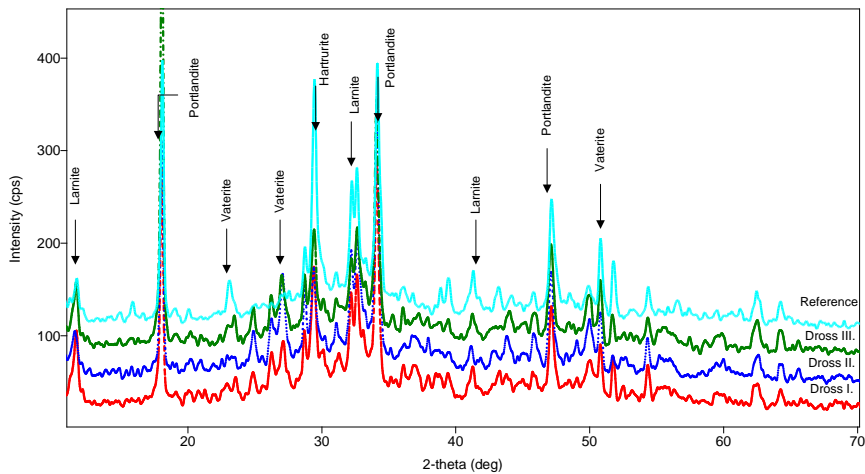
Figure 4
XRD patterns of 28 days concrete foams

2. RESULTS AND DISCUSSION

2.1. Bulk density and porosity

Bulk density results *(Figure 5)* show that adding the treated dross decreases the density of the samples. Dross-free (reference) foamed concrete had the highest bulk density (1,084 kg/m^3). The greatest decrease (13.4%) was seen in foam containing three-washed dross, which was reduced to 939 kg/m^3. Samples containing dross – having a bulk density between 939.5–1,029 kg/m^3 – are in the range of combined lightweight concrete considering that lightweight concretes have the following types: thermal insulating, load bearing and combined (having both thermal insulating and load bearing functions) with bulk density ranges between <200–600 kg/m^3, 600–2,000 kg/m^3 and 600–1,600 kg/m^3, respectively [18].

The AlN in the dross can react with the water as follows [12]:

$$AlN + 3H_2O = Al(OH)_3 + NH_3 \tag{3}$$

$$AlN + 4H_2O = Al(OH)_3 + NH_4OH \tag{4}$$

$$AlN + NaOH + H_2O = NaAlO_2 + NH_3 \tag{5}$$
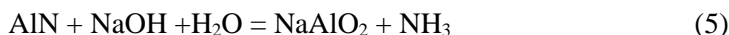
During foaming, a strong pungent odour was smelled that may be caused by the releasing of ammonia. The intense gas releasing reaction could enhance the foaming process.
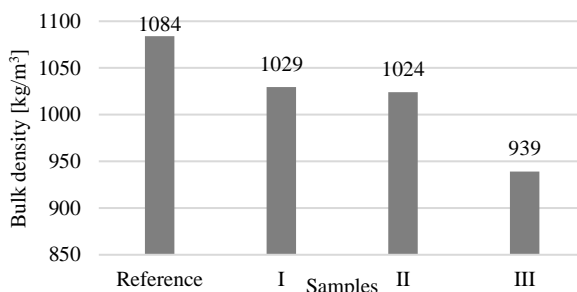
Figure 5
Bulk density of the foamed concretes

Macrographs of the sample are shown on *Figure 6*. Reference, Dross I and II samples have similar structures having pore sizes close to each other. From the pore size measurements *(Table 4)*, it can be concluded that these samples have quite similar mean pore size (0.78, 0.81 and 0.93 mm, respectively). Dross II presented the narrowest pore size distribution. The mean pore size of Dross III was nearly twice as that of any other sample. The minimum and maximum pore size also increased with the number of water leachings.
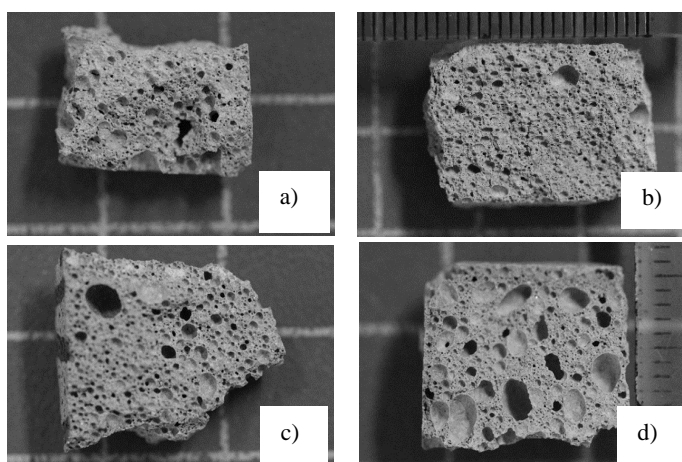
Figure 6
Macrograph of a) Reference (dross-free) b) Dross I c) Dross II d) Dross III sample

Based on the pore size measurements and the macrographs, it can be seen that Dross I and reference sample had dense, homogenous structure. Apart from some big sized pores, Dross II sample also has quite homogenous structure.

Table 4

Average pore size of the foamed concretes

Sample coding	Pore size		
	Mean [mm]	Min [mm]	Max [mm]
Reference	0.78	0.23	2.74
I	0.81	0.17	2.33
II	0.93	0.19	3.11
III	1.72	0.23	3.39

2.2. Thermal conductivity

Thermal conductivity plays an important role in the properties of thermal insulating materials. Results are illustrated on *Figure 7*. Just as the bulk density, reference sample has the highest thermal conductivity (0.07 W/m·K) which means it is the worst insulator among the samples. Dross I and II samples have the same result (0.06 W/m·K), while dross III sample has the lowest value (0.05 W/m·K) meaning it has the best thermal insulating properties. Thermal conductivity and bulk density are directly proportional to each other. Based on our results, these samples meet the requirements of the best thermal insulating concrete.
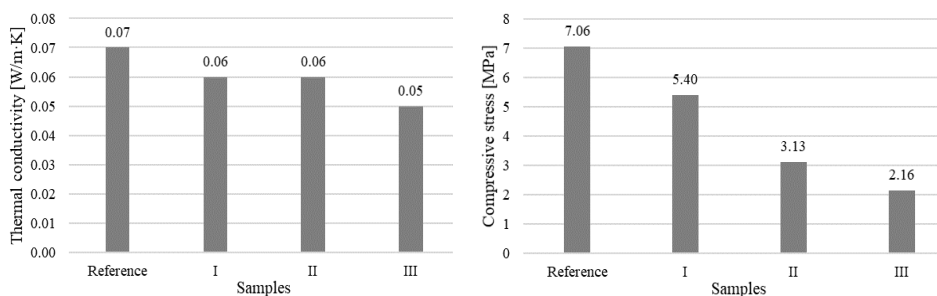
Figure 7

Thermal conductivity and compressive strength of the foamed concretes

2.3. Compressive strength

In case of lightweight concrete, the compressive strength is lower than that of normal concrete, due to the higher porosity and the lower density. Compressive strength of the lightweight concrete ranges from <2.5 to 5.0 MPa and from 5.0 to >15 MPa for thermal insulating and load bearing lightweight concretes, respectively [18]. Strength of the samples *(Figure 7)* varied between 7.1–2.2. MPa. Reference sample had the highest strength (7.1 MPa) which may be due to the denser structure indicated by the higher bulk density. Unlike the density and thermal conductivity results, Dross I and II samples has quite different strength (5.4 and 3.1 MPa, respectively). Lowest strength (2.2

MPa) belongs to dross III sample that corresponds well with the low density. The surface roughness and the specific surface area of the dross particles, which is decreasing with the number of water leaching, may affect the bonding between the cement-dross particles thus the compressive strength of the foam decreases.

Addition of dross unambiguously decreases the strength of the foams, which may be caused by the uncontrolled process of additional gas releasement caused by the reactions of AlN. Reference and Dross I samples meet the aforementioned requirements of load bearing lightweight concretes, while Dross II and III can be qualified to thermal insulators.

2.4. Fractograps

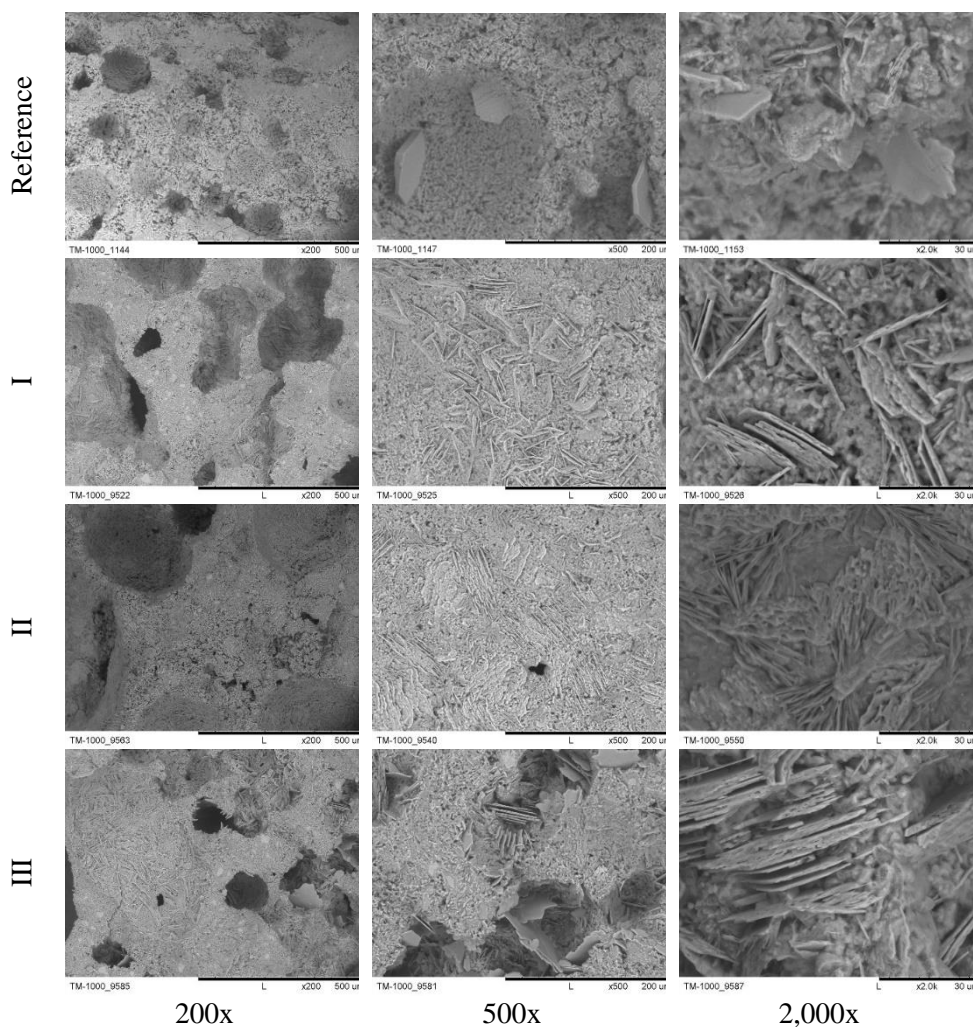
Figure 8
SEM fractographs of concrete foams at 200x, 500x and 2000x magnification

Microstructure of the concrete foams has changed with the number of water leachings *(Figure 8)*.

Both fiber and sheet shaped hydrate products which are typically ettringite and calcium silicate hydrate compounds can be seen. During the hardening of the cement, gypsum was also formed.

CONCLUSION

In this study, the effect of treated aluminum dross on the properties of foamed concrete was investigated. Drosses have been treated with one (I), two (II) or three (III) water leachings before adding to the concrete. Due to the leaching, the initial rough, irregular surface becomes smoother. The main components of the treated drosses were spinel [$MgO \cdot Al_2O_3$], corundum [Al_2O_3] and wurtzit [AlN]. 5 wt% dross as additive and 4 wt% diluted (30 wt%) H_2O_2 as foaming agent were added to the cement slurry. Bulk density, pore size distribution, thermal conductivity and compressive strength tests were performed. Samples containing dross had a bulk density between 939–1,029 kg/m^3 which is lower than that of the reference sample. Reference, Dross I and II samples had similar microstructures with pore sizes close to each other whereas the mean pore size of dross III was nearly twice. Dross I and II samples had the same thermal conductivity (0.06 W/m·K), while dross III sample had the lowest value (0.05 W/m·K). Addition of dross decreases the compressive strength of the foams which may be caused by the decreasing surface roughness and specific surface area of the dross particles affecting disadvantageously the bonding between the cement and dross particles. The additional gas forming caused by the reactions of AlN affected advantageously the bulk density and thermal conductivity of the foams. These results and the requirements of lightweight concretes are summarized in *Table 5*. Addition of dross can result a concrete foam which meets the requirements of load bearing lightweight concrete associated even with better thermal conductivity than that of thermal insulating concrete can present.

Table 5

Requirements of lightweight concretes and their compliance by the foamed concretes (TIC = Thermal insulating concrete, LBC = Load Bearing Concrete)

Required property/ Sample coding	Bulk density [kg/m^3]		Thermal conductivity [W/m·K]		Compressive strength [MPa]	
	TIC	LBC	TIC	LBC	TIC	LBC
	<200–800	800–2,000	<0.06–0.18	0.18–0.8	<2.5–5.0	5.0–>15
Reference	✗	✓1,084	✓0.07	✗	✗	✓7.1
I	✗	✓1,029	✓0.06	✗	✗	✓5.4
II	✗	✓1,024	✓0.06	✗	✓3.1	✗
III	✗	✓939	✓0.05	✗	✓2.2	✗

REFERENCES

[1] *MSZ 4798:2016 Concrete.* Specification, performance, production, conformity, and rules of application of EN 206 in Hungary.

[2] Abdelfattah, M., Kocserha, I., Géber, R. (2019). The effect of calcium fluoride on mineral phases and properties of lightweight expanded clay aggregates. *Proceedings – XIII th International Conference. Preparation of ceramic materials Jahodná*, 25th–27th June, 2019, pp. 141–146. Technical University of Kosice. ISBN 978-80-553-3314-4

[3] Buday, T., Erdélyi, A., Kausay, T. (2007). *Cement-Beton zsebkönyv.* Duna-Dráva Cement Kft.

[4] Zhihua, P., Hengzhi, L., Weiqing, L. (2014). Preparation and characterization of super low density foamed concrete from Portland cement and admixtures. *Construction and Building Materials,* vol. 72, pp. 256–261.

[5] Mohammed, H., Hamad, A. J. (2014). A classification of lightweight concrete: materials, properties and application review. *International Journal of Advanced Engineering Applications*, vol. 7, pp. 52–57.

[6] Dey, V., Bonakdar, A., Mobasher, B. (2014). Low-velocity flexural impact response of fiber-reinforced aerated concrete. *Cement and Concrete Composites*, vol. 49, pp. 100–110.

[7] Souza, M. T., Maykot, C. K., Araújo, A. C. Z., Raupp-Pereira, F., Novaes de Oliveira, A. P. (2017). Electrolytes' influence on foamability and foam stability of cement suspensions. *Construction and Building Materials*, vol. 157, pp. 363–371.

[8] Ramachandran, V. S. (1995). *Concrete Admixtures Handbook: Properties, Science and Technology.* William Andrew Inc.

[9] Hao, L., Wang, R., Zhang, L., Fang, K., Men, Y., Qi, Z., Jiao, P., Tian, J., Liu, J. (2014). Utilizing cellulase as a hydrogen peroxide stabilizer to combine the biopolishing and bleaching procedures of cotton cellulose in one bath. *Cellulose*, vol. 21, no. 1, pp. 777–789.

[10] Peterson, R. D. (2011). A historical perspective on dross processing. *Material Science Forum,* vol. 693, pp .13–23.

[11] Xiao, Y., Reuter, M. A., Boin, U. (2005). Aluminium recycling and environmental issues of salt slag treatment. *Journal of Environmental Science and Health. Part A, Toxic/Hazardous Substances & Environmental Engineering*, vol. 40, pp. 1861–1875.

[12] Hegedűs, B., Kékesi, T. (2018). Leaching behaviour of the residue from the thermomechanical treatment of Aluminum melting dross. *Multiscience XXXII. MicroCAD International Multidisciplinary Scientific Conference*, Miskolci Egyetem, ISBN 978 963 358 162 9, https://doi.org/10.26649/musci.2018.016

[13] Mehta, P. K. (2000). Sulfate attack on concrete: separating myths from reality. *Concrete International*, vol. 22, no. 8, pp. 171–175.

[14] Haynes, H., Bassuoni, M. T. (2011). Physical salt attack on concrete. *Concrete International*, vol. 33, no. 11, pp. 38–42.

[15] St. John, D. A., Poole, A. B., Sims, I. (1998). *Concrete Petrography*. New York: John Wiley & Sons.

[16] Haynes, H., O'Neill, R., Neff, M., Mehta, K. (2010). Salt Weathering of Concrete by Sodium Carbonate and Sodium Chloride. May 2010, *Aci Materials Journal*, 107 (3), pp. 258–266

[17] Illés, I., Sassi, M., Zakiyya,H., Kékesi, T. (2019). The Fundamental Kinetic Characteristics Of Aqueous Dissolution Of Chloride And Fluoride Salts From Secondary Aluminium Dross. in Proceedings of MultiScience - XXXIII. microCAD International Multidisciplinary Scientific Conference, B/3. Miskolci Egyetem, ISBN 978 963 358 177 3, doi: 10.26649/musci.2019.085.

[18] Kausay, T.: Könnyűbeton. http://www.betonopus.hu/notesz/fogalomtar/13-konnyubeton/13-konnyubeton.htm, accessed on 25/05/2019.

EFFECTS OF SPIN-ORBIT INTERACTION
ON SURFACES AND INTERFACES

NÓRA KUCSKA[1]–ZSOLT GULÁCSI[2]

Itinerant 2D two-band systems as surfaces or interfaces are analysed in exact terms in the presence of on-site Coulomb repulsion in the correlated band, and many-body spin-orbit interactions present in both bands. The results show a strong dependence of the particle mobility on the spin-orbit interaction strengths, and also underline that in the high concentration limit, accentuated spin-projection dependence appears in the carrier mobility, which emphasize real application possibilities in spintronics. The spin-projection dependence of the mobility is motivated by the emergence of spontaneous magnetization on the surface, in the presence of spin-orbit interaction, which provide an explication why magnetic properties can appear at the interface of two non-magnetic materials.

Keywords: exact solutions, spin-orbit coupling, strongly correlated systems

INTRODUCTION

Surfaces and interfaces are basic components of main electronic devices controlling and processing the electronic and digital equipment present on a broad spectrum of modern technologies. Indeed, the functionality of semiconducting components, semiconducting and metallic multilayers and interlayers is governed by specially constructed, treated, deposited, configured or formed surfaces and interfaces. On these two dimensional entities, especially in a direction perpendicular to them, potential gradients always appear, which via the Dirac equation introduce the many-body spin-orbit interactions [1] in all processes in which conducting or itinerant carriers play a main role even at non-relativistic level [2]. Often used specific components of this interaction are known as Rashba [3], or Dresselhaus [4] couplings. Written at second quantized level, these provide specific spin-flip type of hopping terms in the one-particle part of the Hamiltonian [5].

Often it happens that many-body processes that take place on surfaces are strongly correlated because usually, given especially by the logarithmic shape of the Coulomb potential in 2D [6], the inter-electronic interactions are strong on surfaces, as in the case of e.g. GaAs heterostructures [7], iridium based heterostructures or iridates [8], perovskites [9], heterostructures with organic materials [10], etc. Contrary to this, the

---

[1] Department of Theoretical Physics, University of Debrecen
    4026 Debrecen, Bem tér 18/a., Hungary
    e-mail address: kucska@phys.unideb.hu
[2] Department of Theoretical Physics, University of Debrecen
    4026 Debrecen, Bem tér 18/a., Hungary
    e-mail address: gulacsi@phys.unideb.hu

spin-orbit many-body coupling strength is small, often 4 order of magnitudes smaller than the highest representative of the Coulomb coupling, namely the on-site repulsion.

But even in this case, the spin-orbit interaction produces essential effects, since being arbitrary small, breaks the spin-projection double degeneracy of each band. As a consequence in this case perturbative treatment, being inconclusive, cannot be applied [11], and consequently the interplay of inter-electronic interactions and spin-orbit coupling is less explored [12], hence is not understood in details [8].

The aim of this paper is to partially fill up this gap. In order to deduce valuable results in conditions in which perturbative treatment cannot be applied, we use exact methods. Since the studied 2D systems are non-integrable, the applied technique is special, and will be presented below.

1. THE USED TECHNIQUE

The used method transforms in the first step in exact terms the system Hamiltonian in positive semidefinite form

$$\hat{H} = \hat{O} + C, \tag{1}$$

where $\hat{O}$ is a positive semidefinite operator, while C is a constant.

Usually, $\hat{O} = \sum_n \hat{O}_n$ is obtained as a sum over positive semidefinite operators $\hat{O}_n$. For a fixed $n = n_1$, the $\hat{O}_{n_1}$ expression can be given e.g. by a construction based on block operators $\hat{A}_{i_{n_1}}$ as $\hat{O}_{n_1} = \hat{A}_{i_{n_1}}{}^{\dagger} \hat{A}_{i_{n_1}}$, or by special expressions as e.g. at $n = n_2$, $\hat{O}_{n_2} = \hat{P}_{n_2} = \hat{n}_{i_{n_1},\uparrow} \hat{n}_{i_{n_1},\downarrow} - (\hat{n}_{i_{n_1},\uparrow} \widehat{+ n}_{i_{n_1},\downarrow}) + 1$. The block operators $\hat{A}_i = \sum_{i,\sigma} p_{j,\sigma} \hat{c}_{j,\sigma}$ are linear combinations of Fermi annihilation operators $\hat{c}_{j,\sigma}$ acting on the sites $j \in B_i$ of a finite block B_i, connected to the site i. The numerical refactors $p_{j,\sigma}$ are block operator parameters.

In order to transform the Hamiltonian in the positive semidefinite form (1), the connected Matching system of equations must be solved. This is obtained because the left side of (1) depends on the Hamiltonian parameters (hopping matrix elements, on-site one-particle potentials, hybridization strengths, etc.), while the right side of (1) is dependent on the block operator parameters and the constant C. Consequently, in order to have the exact identity (1) satisfied, relationships must be present in between the Hamiltonian parameters, the block operator parameters and C.

These equalities build up the Matching system of equations. These equations are usually coupled, non-linear and complex-algebraic equations. Solving them one obtains the explicit expression of the block operator parameters and the constant C.

Once the transformation in positive semidefinite form (1) has been performed, in the second step of the method one deduces the exact multielectronic ground state $|\psi_G\rangle$. Since the minimum possible eigenvalue of a positive semidefinite operator is zero, the exact ground state is provided by the most general solution $|\psi_G\rangle$, of the equation $\hat{O}|\psi_G\rangle = 0$. If necessary, the uniqueness of the solution can also be proved on the line of [13]. The parameter space region in which the deduced ground state is

valid is provided by the parameter domain in which the obtained solution of the Matching system of equations is valid. The ground state energy corresponding to $|\psi_G\rangle$ is provided by the relation $E_G = C$.

In the third step of the method, using the obtained $|\psi_G\rangle$, one calculates the physical properties of the deduced phase by calculating ground state expectation values of different physical quantities of interest.

Also exact results relating the low laying part of the excitation spectrum are possible to be obtained, see [13].

The here presented procedure can be applied always independently on dimensionality and integrability. The technical steps necessary to be used in the presented first two steps have been worked out in extreme details [13–16], and the procedure has been successfully applied before in several many-body cases of large interest, including three dimensions [17], two dimensional disordered systems [18], or stripes, checkerboards and droplets in 2D [19]. The novelty in using the method in the present case is that in transforming the Hamiltonian in positive semidefinite form, two block operators are used containing the components of both spin projections of fermionic carriers.

The remaining part of the paper is structured as follows: Sect. II presents the studied system, Sect. III describes the obtained results, Sect. IV. concludes the paper, and the Appendix containing the mathematical details closes the presentation.

2. THE STUDIED SYSTEM

One analyses a realistic itinerant surface or interface which is always of multiband type. For multiband materials the theoretical description is given usually by projecting the multiband structure in a few-band picture present around the Fermi surface [20], projection which is stopped here for its workability, at two-band level. One of these bands (denoted conventionally by f) is considered correlated, while the second band (denoted formally by d) is taken into account in a non-correlated form. In between these bands, as in real materials, hybridization is present whose strength is denoted by V.

Also for its simplicity, one considers here a 2D orthorhombic Bravais lattice present on the surface. Concerning the inter-electronic interaction, given by the strong screening present in itinerant many-body systems, one takes into account the main component of the Coulomb interaction in such cases, namely the on-site Coulomb repulsion U_f present in the correlated band. The hopping matrix elements are denoted by t, while the on-site one-particle potentials by ε. The Hamiltonian of the system is given by $\hat{H} = \hat{H}_{kin} + \hat{H}_{int} + \hat{H}_{SO}$, where

$$\hat{H}_{c,0} = \sum_i \sum_{\alpha=\uparrow,\downarrow} \varepsilon_c \, \hat{c}_{i,\alpha}^\dagger \hat{c}_{i,\alpha}, \quad \hat{V}_0 = \sum_i \left[\left(\sum_{\alpha=\uparrow,\downarrow} V_0^{d,f} \, \hat{d}_{i,\alpha}^\dagger \hat{f}_{i,\alpha} \right) + H.c. \right],$$

$$\hat{H}_{c,p} = \sum_i \left[\left(\sum_{\alpha=\uparrow,\downarrow} t_p^c \hat{c}_{i+p,\alpha}^\dagger \hat{c}_{i,\alpha} \right) + H.c. \right],$$

$$\hat{V}_p = \sum_i \left[\left(\sum_{\alpha=\uparrow,\downarrow} V_p^{d,f} \hat{d}_{i+p,\alpha}^\dagger \hat{f}_{i,\alpha} + V_p^{f,d} \hat{f}_{i+p,\alpha}^\dagger \hat{d}_{i,\alpha} \right) + H.c. \right],$$

$$\hat{H}_{kin} = \hat{V}_0 + \sum_{c=d,f} \hat{H}_{c,0} + \sum_{p=x,y} \left[\hat{V}_p + \sum_{c=d,f} \hat{H}_{c,p} \right], \quad \hat{H}_{int} = \sum_i U_f \, \hat{n}_{i,\uparrow}{}^f \hat{n}_{i,\downarrow}{}^f,$$

$$\hat{H}_{SO} = \sum_{c=d,f} \sum_i \left[\sum_{p=x,y} (t_{\uparrow,\downarrow}^{c,p} \hat{c}_{i+p,\uparrow}^\dagger \hat{c}_{i,\downarrow} + t_{\downarrow,\uparrow}^{c,p} \hat{c}_{i+p,\downarrow}^\dagger \hat{c}_{i,\uparrow}) + H.c. \right],$$

$$(2)$$

where $p = x, y$ are the Bravais vectors of the system, $\hat{n}_{i,\alpha}{}^f = \hat{f}_{i,\alpha}{}^\dagger \hat{f}_{i,\alpha}$, . Note that the spin-orbit coupling enters in $\hat{H}_{SO,c}$, where $c = d, f$, $p = x, y$ and one has $t_{\uparrow,\downarrow}^{c,x} = t_R^c - it_D^c$, $t_{\downarrow,\uparrow}^{c,x} = -t_R^c - it_D^c$, $t_{\uparrow,\downarrow}^{c,y} = t_D^c - it_R^c$, $t_{\downarrow,\uparrow}^{c,y} = -t_D^c - it_R^c$, where represents $t_R^c, (t_D^c)$ the Rashba (Dresselhaus) interaction strength.

3. THE OBTAINED RESULTS

For the transformation into positive semidefinite form two block operators have been used defined on the unit cell connected to the lattice site i.

$$\hat{A}_i = \sum_{c=d,f} \sum_{\alpha=\uparrow,\downarrow} (a_{c,1,\alpha} \, \hat{c}_{i,\alpha} + a_{c,2,\alpha} \hat{c}_{i+x,\alpha} + a_{c,3,\alpha} \hat{c}_{i+x+y,\alpha} + a_{c,4,\alpha} \hat{c}_{i+y,\alpha}),$$

$$\hat{B}_i = \sum_{c=d,f} \sum_{\alpha=\uparrow,\downarrow} (b_{c,1,\alpha} \, \hat{c}_{i,\alpha} + b_{c,2,\alpha} \hat{c}_{i+x,\alpha} + b_{c,3,\alpha} \hat{c}_{i+x+y,\alpha} + b_{c,4,\alpha} \hat{c}_{i+y,\alpha}).$$

$$(3)$$

The Hamiltonian transformed into a positive semidefinite form as mentioned above has the expression $\hat{H} = \hat{O} + C$, where $\hat{O} = \hat{O}_1 + \hat{O}_2$.

$$\hat{O}_2 = \sum_i (\hat{A}_i \hat{A}_i^\dagger + \hat{B}_i \hat{B}_i^\dagger), \quad \hat{O}_1 = U_f \sum_i \hat{P}_{i,}$$

$$C = \eta N - U_f N_{sit} - \sum_i (z_i^A + z_i^B), z_i^A = \left\{ \hat{A}_i, \hat{A}_i^\dagger \right\}, z_i^B = \left\{ \hat{B}_i, \hat{B}_i^\dagger \right\},$$

$$(4)$$

where N represents the number of electrons, N_{sit} gives the number of lattice sites. After solving the connected Matching system of equations one obtains the explicit expression of the block operator parameters and η presented in the Appendix.

The exact ground state corresponding to the positive semidefinite form of the Hamiltonian has the expression

$$|\psi_G(N = N^*)\rangle = \prod_i [\hat{A}_i^\dagger \hat{B}_i^\dagger (\hat{f}_{i,\uparrow}^\dagger + \hat{f}_{i,\downarrow}^\dagger)]|0\rangle$$

(5)

where $|0\rangle$ represents the bare vacuum with no fermions present, and the product over i extends over all lattice sites. The presented ground state corresponds to the electron number $N = N^*$, where N^* is three times the number of lattice sites in the system ($N^* = 3N_{sit}$). For $N = N_1 + N^*$ the right side of (1) has to extend with a new operator, and a similar expression exists also for the case $N < \frac{N^*}{3}$.

Based on the obtained ground state wave function we deduced the long-range hopping ground state expectation value of $\hat{\Gamma}_{r,c,\sigma} = \frac{1}{N_{sit}}\sum_j(\hat{c}_{j,\sigma}^\dagger \hat{c}_{j+r,\sigma} + H.c.)$. This quantity was calculated for $c = d$ and in x direction, as can be seen in *Figure 1*. It shows a strong spin projection and spin-orbit coupling strength dependence. This remains true for arbitrary direction, and is motivated by the nonzero value of the ground state expectation value of the total spin $\hat{S}_z$ operator, signaling the emergence of spontaneous magnetization on the surface in the presence of spin-orbit coupling in the studied case. Since the long-range hopping determines the mobility of particles, the enumerated properties remain true also for the carrier mobility.
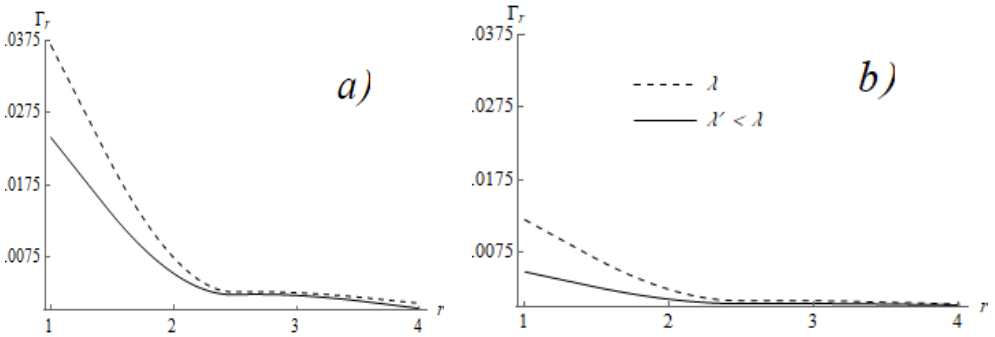
Figure 1

The r dependent hopping ground state expectation value Γ_r in function of the effective spin-orbit interaction $\lambda = \frac{1}{2}\sum_{c=d,f}\sqrt{(t_D^c)^2 + (t_R^c)^2}$ exemplified for d electrons in x direction. The distance r is given in lattice constant units. In the plot one has in t_x^f units $\lambda = 0.0603$, and $\lambda' = 0.0307$ respectively. Note that if λ increases, Γ_r increases as well and one has a strong spin projection dependence. The presented cases: a) negative spin projection to the Z axis, b) positive spin projection to the Z axis.

CONCLUSION

Realistic itinerant surfaces with inter-electronic on-site Coulomb repulsion and many-body spin-orbit interactions have been described in exact terms using a technique based on positive semidefinite operator properties. The method can always be applied for many-body systems independent on dimensionality and integrability. The Hamiltonian containing only local and nearest-neighbour terms has been transformed in positive semidefinite form, the exact ground state has been deduced, and ground state properties analysed. In the high concentration limit a strong dependence of the carrier mobility on spin projection and the strength of the spin-orbit interaction has been observed together with the emergence of ferromagnetism on the surface.

ACKNOWLEDGEMENT

APPENDIX

This appendix presents the explicitly deduced block operator parameters.

$$b_{1,f,\uparrow} = \sqrt{\frac{(|v|-1)^2}{2\sqrt{2}(|v|+1)^2} \frac{|v|}{|u|}} \sqrt{\Theta_\uparrow} e^{i(\gamma+\phi_u+\delta_\uparrow)/2} \, ,$$

$$b_{1,f,\downarrow} = \sqrt{\frac{(|v|-1)^2}{2\sqrt{2}(|v|+1)^2} \frac{|v|}{|u|}} \sqrt{\Theta_\downarrow} e^{i(-\gamma+\phi_u+\delta_\downarrow)/2} \, ,$$

$$b_{2,f,\uparrow} = \frac{v\sqrt{2}}{|(|v|-1)|} \sqrt{\frac{(|v|-1)^2}{2\sqrt{2}(|v|+1)^2} \frac{|v|}{|u|}} \sqrt{\Theta_\downarrow} e^{i(\phi_u+\delta_\downarrow)/2},$$

$$b_{2,f,\downarrow} = \frac{v\sqrt{2}}{|(|v|-1)|} \sqrt{\frac{(|v|-1)^2}{2\sqrt{2}(|v|+1)^2} \frac{|v|}{|u|}} \sqrt{\Theta_\uparrow} e^{i(\phi_u+\delta_\uparrow)/2} \, ,$$

$$b_{3,f,\uparrow} = -\frac{1}{x^*} \sqrt{\frac{(|v|-1)^2}{2\sqrt{2}(|v|+1)^2} \frac{|v|}{|u|}} \sqrt{\Theta_\uparrow} e^{i\frac{(\gamma+\phi_u+\delta_\uparrow+2\phi)}{2}} \, ,$$

$$b_{3,f,\downarrow} = \frac{1}{x^*} \sqrt{\frac{(|v|-1)^2}{2\sqrt{2}(|v|+1)^2} \frac{|v|}{|u|}} \sqrt{\Theta_\downarrow} e^{i\frac{(-\gamma+\phi_u+\delta_\downarrow+2\phi)}{2}} \, ,$$

$$b_{4,f,\uparrow} = -\frac{1}{v^*}\frac{v\sqrt{2}}{|(|v|-1)|}\sqrt{\frac{(|v|-1)^2}{2\sqrt{2}(|v|+1)^2}\frac{|v|}{|u|}}\sqrt{\Theta_\uparrow}e^{i\frac{(\phi_u+\delta_\uparrow+2\phi)}{2}},$$

$$b_{4,f,\downarrow} = \frac{1}{v^*}\frac{v\sqrt{2}}{||v|-1|}\sqrt{\frac{(|v|-1)^2}{2\sqrt{2}(|v|+1)^2}\frac{|v|}{|u|}}\sqrt{\Theta_\downarrow}e^{i\frac{(\phi_u+\delta_\downarrow+2\phi)}{2}},$$

$$b_{1,d,\uparrow} = \frac{u_\uparrow}{v}\sqrt{\frac{(|v|-1)^2}{2\sqrt{2}(|v|+1)^2}\frac{|v|}{|u|}}\sqrt{\Theta_\downarrow}e^{-i\frac{(-\gamma+\phi_u+\delta_\downarrow+2\phi)}{2}},$$

$$b_{1,d,\downarrow} = -\frac{u_\downarrow}{v}\sqrt{\frac{(|v|-1)^2}{2\sqrt{2}(|v|+1)^2}\frac{|v|}{|u|}}\sqrt{\Theta_\uparrow}e^{-i\frac{(\gamma+\phi_u+\delta_\uparrow+2\phi)}{2}},$$

$$b_{2,d,\uparrow} = \frac{u_\uparrow}{v}\frac{v^*\sqrt{2}}{||v|-1|}\sqrt{\frac{(|v|-1)^2}{2\sqrt{2}(|v|+1)^2}\frac{|v|}{|u|}}\sqrt{\Theta_\downarrow}e^{-i\frac{(\phi_u+\delta_\downarrow+2\phi)}{2}},$$

$$b_{2,d,\downarrow} = -\frac{u_\downarrow}{v}\frac{v^*\sqrt{2}}{|(|v|-1)|}\sqrt{\frac{(|v|-1)^2}{2\sqrt{2}(|v|+1)^2}\frac{|v|}{|u|}}\sqrt{\Theta_\uparrow}e^{-i\frac{(\phi_u+\delta_\uparrow+2\phi)}{2}},$$

$$b_{3,d,\uparrow} = -\frac{u_\uparrow}{vx^*}\sqrt{\frac{(|v|-1)^2}{2\sqrt{2}(|v|+1)^2}\frac{|v|}{|u|}}\sqrt{\Theta_\downarrow}e^{-i\frac{(-\gamma+\phi_u+\delta_\downarrow)}{2}},$$

$$b_{3,d,\downarrow} = -\frac{u_\downarrow}{vx^*}\sqrt{\frac{(|v|-1)^2}{2\sqrt{2}(|v|+1)^2}\frac{|v|}{|u|}}\sqrt{\Theta_\uparrow}e^{-i\frac{(\gamma+\phi_u+\delta_\uparrow)}{2}},$$

$$b_{4,d,\downarrow} = -\frac{u_\downarrow}{v}\frac{\sqrt{2}}{|(|v|-1)|}\sqrt{\frac{(|v|-1)^2}{2\sqrt{2}(|v|+1)^2}\frac{|v|}{|u|}}\sqrt{\Theta_\downarrow}e^{-i\frac{(\phi_u+\delta_\downarrow)}{2}},$$

$$b_{4,d,\uparrow} = -\frac{u_\uparrow}{v}\frac{\sqrt{2}}{||v|-1|}\sqrt{\frac{(|v|-1)^2}{2\sqrt{2}(|v|+1)^2}\frac{|v|}{|u|}}\sqrt{\Theta_\uparrow}e^{-i\frac{(\phi_u+\delta_\uparrow)}{2}}.$$

$$a_{1,f,\uparrow} = -\frac{1}{x}\sqrt{\frac{(|v|-1)^2}{2\sqrt{2}(|v|+1)^2}\frac{|v|}{|u|}}\sqrt{\Theta_\uparrow}e^{i(\gamma+\phi_u+\delta_\uparrow)/2},$$

$$a_{1,f,\downarrow} = -\frac{1}{x}\sqrt{\frac{(|v|-1)^2}{2\sqrt{2}(|v|+1)^2}\frac{|v|}{|u|}}\sqrt{\Theta_\downarrow}e^{i(-\gamma+\phi_u+\delta_\downarrow)/2},$$

$$a_{2,f,\uparrow} = -\frac{\sqrt{2}}{|(|v|-1)|}\sqrt{\frac{(|v|-1)^2}{2\sqrt{2}(|v|+1)^2}\frac{|v|}{|u|}}\sqrt{\Theta_\downarrow}e^{i(\phi_u+\delta_\downarrow)/2},$$

$$a_{2,f,\downarrow} = -\frac{\sqrt{2}}{|(|v|-1)|}\sqrt{\frac{(|v|-1)^2}{2\sqrt{2}(|v|+1)^2}\frac{|v|}{|u|}}\sqrt{\Theta_\uparrow}e^{i(\phi_u+\delta_\uparrow)/2},$$

$$a_{3,f,\uparrow} = -\sqrt{\frac{(|v|-1)^2}{2\sqrt{2}(|v|+1)^2}\frac{|v|}{|u|}}\sqrt{\Theta_\uparrow}e^{i\frac{(\gamma+\phi_u+\delta_\uparrow+2\phi)}{2}},$$

$$a_{3,f,\downarrow} = \sqrt{\frac{(|v|-1)^2}{2\sqrt{2}(|v|+1)^2}\frac{|v|}{|u|}}\sqrt{\Theta_\downarrow}e^{i\frac{(-\gamma+\phi_u+\delta_\downarrow+2\phi)}{2}},$$

$$a_{4,f,\uparrow} = -\frac{v\sqrt{2}}{|(|v|-1)|}\sqrt{\frac{(|v|-1)^2}{2\sqrt{2}(|v|+1)^2}\frac{|v|}{|u|}}\sqrt{\Theta_\uparrow}e^{i\frac{(\phi_u+\delta_\uparrow+2\phi)}{2}},$$

$$a_{4,f,\downarrow} = \frac{v\sqrt{2}}{||v|-1|}\sqrt{\frac{(|v|-1)^2}{2\sqrt{2}(|v|+1)^2}\frac{|v|}{|u|}}\sqrt{\Theta_\downarrow}e^{i\frac{(\phi_u+\delta_\downarrow+2\phi)}{2}},$$

$$a_{1,d,\uparrow} = -\frac{u_\uparrow}{xv}\sqrt{\frac{(|v|-1)^2}{2\sqrt{2}(|v|+1)^2}\frac{|v|}{|u|}}\sqrt{\Theta_\downarrow}e^{-i\frac{(-\gamma+\phi_u+\delta_\downarrow+2\phi)}{2}},$$

$$a_{1,d,\downarrow} = \frac{u_\downarrow}{xv}\sqrt{\frac{(|v|-1)^2}{2\sqrt{2}(|v|+1)^2}\frac{|v|}{|u|}}\sqrt{\Theta_\uparrow}e^{-i\frac{(\gamma+\phi_u+\delta_\uparrow+2\phi)}{2}},$$

$$a_{2,d,\uparrow} = -\frac{u_\uparrow}{v^2}\frac{v^*\sqrt{2}}{||v|-1|}\sqrt{\frac{(|v|-1)^2}{2\sqrt{2}(|v|+1)^2}\frac{|v|}{|u|}}\sqrt{\Theta_\downarrow}e^{-i\frac{(\phi_u+\delta_\downarrow+2\phi)}{2}},$$

$$a_{2,d,\downarrow} = \frac{u_\downarrow}{v^2}\frac{v^*\sqrt{2}}{|(|v|-1)|}\sqrt{\frac{(|v|-1)^2}{2\sqrt{2}(|v|+1)^2}\frac{|v|}{|u|}}\sqrt{\Theta_\uparrow}e^{-i\frac{(\phi_u+\delta_\uparrow+2\phi)}{2}},$$

$$a_{3,d,\uparrow} = -\frac{u_\uparrow}{v}\sqrt{\frac{(|v|-1)^2}{2\sqrt{2}(|v|+1)^2}\frac{|v|}{|u|}}\sqrt{\Theta_\downarrow}e^{-i\frac{(-\gamma+\phi_u+\delta_\downarrow)}{2}},$$

$$a_{3,d,\downarrow} = -\frac{u_\downarrow}{v}\sqrt{\frac{(|v|-1)^2}{2\sqrt{2}(|v|+1)^2}\frac{|v|}{|u|}}\sqrt{\Theta_\uparrow}e^{-i\frac{(\gamma+\phi_u+\delta_\uparrow)}{2}},$$

$$a_{4,d,\downarrow} = -\frac{u_\downarrow}{v}\frac{v^*\sqrt{2}}{|(|v|-1)|}\sqrt{\frac{(|v|-1)^2}{2\sqrt{2}(|v|+1)^2}\frac{|v|}{|u|}}\sqrt{\Theta_\downarrow}e^{-i\frac{(\phi_u+\delta_\downarrow)}{2}},$$

$$a_{4,d,\uparrow} = -\frac{u_\uparrow}{v}\frac{v^*\sqrt{2}}{||v|-1|}\sqrt{\frac{(|v|-1)^2}{2\sqrt{2}(|v|+1)^2}\frac{|v|}{|u|}}\sqrt{\Theta_\uparrow}e^{-i\frac{(\phi_u+\delta_\uparrow)}{2}}.$$

Here $\gamma, u_\sigma, \sigma = \uparrow, \downarrow$ are arbitrary ($\neq 0, \infty$) numerical parameters, $v = |v|e^{i\phi_u}$, $x = |x|e^{i\phi_u}$ and $|x| = \frac{|v|-1}{|v|+1}$. The $\frac{|v|}{|u|}$ ratio and the $\delta_\uparrow - \delta_\downarrow$ phase (with the choise $\chi = \phi_u + \phi = \frac{\pi}{2}$) can be expressed as

$$\frac{|v|}{|u|} = \frac{-t_x^f}{\sqrt{\Theta_\uparrow\Theta_\downarrow}\cos\frac{\delta_\uparrow-\delta_\downarrow}{2}}, \qquad \tan\frac{\delta_\uparrow-\delta_\downarrow}{2} = \frac{t_y^f}{t_x^f}.$$

A
lso η is obtainable via ε_f

$$\eta = \varepsilon_f + U_f - 4\frac{1+|v|^2}{(|v|-1)^2}\left(\left|b_{1,f,\uparrow}\right|^2 + \left|b_{1,f,\downarrow}\right|^2\right).$$

REFERENCES

[1] Spavieri, G., Mansuripur, M. (2015). Origin of the spin–orbit interaction. *Physica Scripta*, vol. 90, no. 8, p. 085501, June 2015 [online]. Available: https://iopscience.iop.org/article/10.1088/0031-8949/90/8/085501/meta

[2] Baym, G. (1973). *Lectures on quantum mechanics*. Chapter 23, Benjamin-Cummings Publishing Co.

[3] Bychkov, Y. A., Rashba, E. I. (1984). Properties of a 2D Electron Gas with Lifted Spectral Degeneracy. *JETP Letters*, vol. 39, no. 2, pp. 78–83 [online]. Available: http://www.jetpletters.ac.ru/ps/1264/article_19121.shtml

[4] Dresselhaus, G. (1955). Spin-Orbit Coupling Effects in Zinc Blende Structures. *Phys. Rev.*, vol. 100, no. 2, pp. 580–586, October 1955 [online]. Available: https://link.aps.org/doi/10.1103/PhysRev.100.580.

[5]   Li, Z., Covaci, L., Marsiglio, F. (2012). Impact of Dresselhaus versus Rashba spin-orbit coupling on the Holstein polaron. *Phys. Rev. B.*, vol. 85, no. 20, p. 205112, May 2012 [online]. Available: https://link.aps.org/doi/10.1103/Phys RevB.85.205112.

[6]   Kosterlitz, J. M., Thouless, D. J. (1973). Ordering, metastability and phase transitions in two-dimensional systems. *Journal of Physics C: Solid State Physics*, vol. 6, no. 7, p. 1181 [online]. Available: https://doi.org/10.1088/00 22-3719/6/7/010.

[7]   Huang, J., Pfeiffer, L. N., West, K. W. (2017). Spin-orbit coupling and transport in strongly correlated two-dimensional systems. *Phys. Rev. B*, vol. 95, no. 19, p. 195139, May 2017 [online]. Available: https://link.aps.org/doi/10.1103/PhysRevB.95.195139.

[8]   Shaffer, R., Lee, E. K. H., Yang, B. J., Kim, Y. B. (2016). Recent progress on correlated electron systems with strong spin–orbit coupling. *Reports on Progress in Physics*, vol. 79, no 9, p. 094504, August 2016 [online]. Available: https://doi.org/10.1088/0034-4885/79/9/094504.

[9]   Brinkman, A., Huiben, M., van Zalk, M. et al. (2007). Magnetic effects at the interface between non-magnetic oxides. *Nat. Matter*, vol. 6, p. 493, June 2007 [online]. Available: https://www.nature.com/articles/nmat1931.

[10] Raman, K. V., Moodera, J. S. (2015). A magnetic facelift for non-magnetic metals. *Nature*, vol. 524, p. 42, August 2015 [online].
      Available: https://www.nature.com/articles/524042a.

[11] Raul, J. G., Lee, E. K. H., Kee, H. Y. (2015). Spin-Orbit Physics Giving Rise to Novel Phases in Correlated Systems: Iridates and Related Materials. *Annual Review of Condensed Matter Physics*, vol. 7, p. 195, December 2015 [online]. Available: https://doi.org/10.1146/annurev-conmatphys-031115-011319.

[12] Gangopadhyay, S., Pickett, W. E. (2016). Spin-orbit coupling, strong correlation, and insulator-metal transitions: The $J_{eff} = \frac{3}{2}$ ferromagnetic Dirac-Mott insulator $Ba_2 NaOsO_6$. *Phys. Rev. B*, vol. 93, no. 4, p. 155126, January 2016 [online]. Available: https://link.aps.org/doi/10.1103/PhysRevB.91.045133

[13] Gulácsi, Z. (2013). Exact ground states of correlated electrons on pentagon chains. *International Journal of Modern Physics B*, vol. 27, no. 14, p. 1330009, May 2013 [online]. Available: http://doi.org/10.1142/S0217979213300090.

[14] Gulácsi, Z., Vollhardt, D. (2003). Exact Insulating and Conducting Ground States of a Periodic Anderson Model in Three Dimensions. *Phys. Rev. Lett.*, vol. 91, no. 18, p. 186401, October 2003 [online]. Available: http://link.aps.org/doi/10.1103/PhysRevLett.91.186401.

[15] Gulácsi, Z., Kampf, A., Vollhardt, D. (2007). Exact Many-Electron Ground States on the Diamond Hubbard Chain. *Phys. Rev. Lett.*, vol. 99, no. 2, p. 026404, July 2007 [online]. Available: http://link.aps.org/doi/10.1103/Phys RevLett.99.026404.

[16] Gulácsi, Z., Kampf, A., Vollhardt, D. (2010). Route to Ferromagnetism in Organic Polymers. *Phys. Rev. Lett.*, vol. 105, no. 26, p. 266403, December 2010 [online]. Available: http://link.aps.org/doi/10.1103/PhysRevLett.105.266403.

[17] Gulácsi, Z., Vollhardt, D. (2005). Exact ground states of the periodic Anderson model in D = 3 dimensions. *Phys. Rev. B*, vol. 72, no. 7, p. 075130, August 2005 [online]. Available: http://link.aps.org/doi/10.1103/PhysRevB. 72.075130.

[18] Gulácsi, Z. (2004). Exact multielectronic electron-concentration-dependent ground states for disordered two-dimensional two-band systems in the presence of disordered hoppings and finite on-site random interactions. *Phys. Rev. B*, vol. 69, no. 5, p. 054204, February 2004 [online].
Available: http://link.aps.org/doi/10.1103/PhysRevB.69.054204.

[19] Gulácsi, Z., Gulácsi, M. (2006). Exact stripe, checkerboard, and droplet ground states in two dimensions. *Phys. Rev. B*, vol. 73, no. 1, p. 014524, January 2006 [online]. Available: http://link.aps.org/doi/10.1103/PhysRevB.73.014524.

[20] Kollar, M., Strack, R., Vollhardt, D. (1996). Ferromagnetism in correlated electron systems: Generalization of Nagaoka's theorem. *Phys. Rev. B*, vol. 53, no. 14, p. 9225, April 1996 [online]. Available: http://link.aps.org/doi/10.11 03/PhysRevB.53.9225.

INVESTIGATION OF AIR POLLUTANTS
FROM RESIDENTIAL HEATING

DÓRA MENTES[1]–HELGA KOVÁCS[2]–
GÁBOR NAGY[3]–CSABA PÓLISKA[4]

Beside of industry, agriculture, and transport, primarily the solid combustion plants used by households are responsible for the emission of gaseous and solid pollutants in ambient air. Thus, the actual reduction of air pollutant concentration also can be achieved by regulating of residential heating. New, solid-fired, individual room heating systems will have to meet stricter emission requirements from 1 January 2022. People in poorer regions are not able to buy new equipment, so in most households old equipments in poor condition remain in use. In addition, the population – albeit illegal – in most cases also burn the combustible waste generated in the households in their stove or boiler, which further increases the amount of air pollutant emissions. So far the authorities cannot be to clearly demonstrate the combustion of waste from the flue gas and residual ash, because these methods are expensive and hardly unworkable, as the authorities find it difficult to get into private homes.

Keywords: the limit value of air pollutants, emissions factors of combustion equipment, residential heating

INTRODUCTION

The harmful effects of air pollution on health and the environment are well known. In Europe, greenhouse gas emissions have declined significantly over the past decades, resulting in improved air quality in the region, but still the concentrations of air pollutants are high [1]. According to World Health Organization (WHO) and European Economic Area (EEA), this reduction in total emissions of air pollutants does not automatically lead to a similar reduction in air pollutant concentrations [2].

Most of European population live in a place – mainly in cities – where the air pollution exceeds the air quality limits at certain regular intervals: the NO_2 and particulate matter pollution pose a serious health risk [1]. The laws do not place any

[1]   Department of Combustion Technology and Thermal Energy, University of Miskolc
       H-3515 Miskolc-Egyetemváros, Hungary
       tuzdora@uni-miskolc.hu
[2]   Department of Combustion Technology and Thermal Energy, University of Miskolc
       H-3515 Miskolc-Egyetemváros, Hungary
       kovacs.helga@uni-miskolc.hu
[3]   Department of Combustion Technology and Thermal Energy, University of Miskolc
       H-3515 Miskolc-Egyetemváros, Hungary
       nagy.gabi@uni-miskolc.hu
[4]   Department of Combustion Technology and Thermal Energy, University of Miskolc
       H-3515 Miskolc-Egyetemváros, Hungary
       tuzcsaba@uni-miskolc.hu

emphasis on reducing emissions where people are most affected by air pollution and where the highest concentrations are [2].

The European Union has initiated infringement proceedings against Hungary for persistent exceedances of particulate matter levels and NO_2 levels. NO_2 is mainly presented in emissions from industry, transport, domestic heating, and agriculture. Limit exceedances occur predominantly during the heating season and are mainly resulted of the solid firing by the public [3].

The effect of air pollutant from household solid combustion plants is influenced by three circumstances:
  • condition of the combustion plant and chimney,
  • quality of fuel used,
  • firing method applicable to the equipment.

In the past decade, especially in the poorer sections of society, many households have returned for the use of solid fuel equipment instead of their gas-fired heating systems because of economic reasons [4]. The population has no acceptable information and knowledge of how and what way operate their boilers correctly. Regardless of the age and type of the boilers, in the absence of proper knowledge, combustion is imperfect, which further increases pollution.

In poor households, as they are unable to buy the right quality fuel, besides solid fuels the household wastes are also thrown into the boiler. In the case of incomplete combustion, along with the increase in the amount of harmful flue gas components and flue dust, also the growth the amount of polycyclic aromatic hydrocarbons (PAH) content have to be taken into account.

1. QUANTITY AND LIMITS OF AIR POLLUTANTS IN HUNGARY

Free atmospheric tests are called immission measurements, or air quality tests too, and investigation of air pollutants from point sources are called emission measurements. [5].

Limit values for air pollutants affecting ambient air quality are given in "4/2011. (I. 14.) Decree of the Ministry of Rural Development on limit values for air load level and emission limit values for stationary air pollution point sources" *(Table 1)*.

The concentration of benzo[a]pyrene should be determined as the annual average of the total quantity in the PM10 fraction [6]. In 1984, the United States Environmental Protection Agency (EPA) appraised the risks posed by PAH mixtures with the assumption that all carcinogenic PAHs have the same environmental effects as benzo[a]pyrene. [7]. Several studies disagree with the fact that benzo[a]pyrene is used as an indicator of the carcinogenic risk of atmospheric polycyclic aromatic compounds, as benzo[a]pyrene amount is highly more dependent on the sunlight, temperature, and the amount of NO_x, SO_2, O_3 than the amount of other polycyclic aromatic hydrocarbons [8], [9].

The CO and NO_2 concentration in the atmosphere showed a slight decrease between 2013 and 2016 *(Figure 1)*. PM2.5 and PM10 have remained almost constant since 2013, while CO_2 emissions have increased since 2014.

Table 1

Limit values for pollutants emitted to ambient air in Hungary [6]

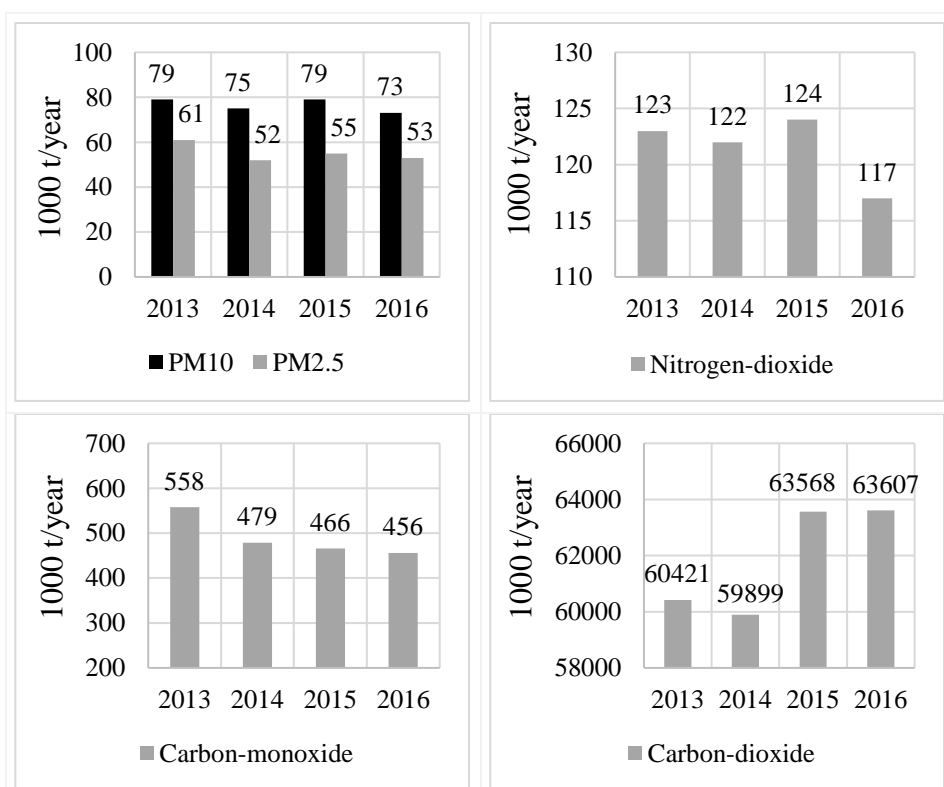| Pollutant	Limit values [µg/m³]		
	24 h PM10	**Annual PM10**	**Annual PM2.5**
PM10/PM2.5	50 up to 35 times a calendar year	40	24
	1 h	24 h	Annual
NO$_2$	100 up to 18 times a calendar year	85	40
	1 h	24 h	Annual
CO	10,000	5,000	3,000
	24 h	Annual	
Benzo[a]pyrene	0.001	0.0012	

Figure 1

Quantity of pollutants emitted into the air in Hungary [thousand tons/year]
[10], [11]

In 2016, households released the largest share of CO_2 (37% of total emissions), followed by the energy sector (23%). Nearly two-thirds of PM10 is emitted into the atmosphere from residential heating *(Table 2)*. More than 85% of the total emissions of CO and PM2.5 come from the households. Households, agriculture, and transport are equally responsible for emissions of NO_2.

Table 2

Percentage distribution of air pollutant emissions from Sectors in 2016 in Hungary [10], [12], [13], [14], [15]

Sectors	CO$_2$	CO	PM10	PM2.5	NO$_2$
	[m/m%]				
Households	36.58	86.99	65.73	87.62	20.91
Energy sector	23.27	1.72	0.35	0.41	8.75
Manufacturing industry	17.56	5.12	2.86	2.92	11.28
Transport	6.94	2.14	1.98	2.11	19.09
Agriculture	3.82	1.07	14.06	2.54	22.38
Building Industry	1.67	0.43	10.02	1.79	3.33

According to the website of the National Air Pollution Network, in Hungary 51 monitoring and 3 background stations operate within the framework of the National Air Pollution Measurement Network. Most environmental authorities have mobile stations, including the B.-A.-Z. County Environmental Authority, which has two mobile stations. Taking into consideration all air pollutants, the number of stations with qualification "appropriate" and "contaminated" ratings increased in 2017 compared to 2016, and the number of "good" qualificated stations decreased. Since 2015, the "heavily polluted" rating has not been given to a monitoring station [16].

The exceedance of average annual limit of PM10 concentration was measured at one station in 2015, while in 2017 at three stations, of which two stations are in the Sajó Valley (Miskolc and Sajószentpéter). In the case of NO_2 concentration, starting from 2013, two stations continuously exceed the annual limits (Pécs, Szabadság Road; Budapest, Széna Square) [16]. *Figure 2* shows the annual average values of air pollutants in Miskolc.

In addition to the annual limits, many daily and hourly limits are determined. As stated in the regulation, the PM10 concentration in a calendar year should not exceed the daily limit more than 35 occasions. Between 2014 and 2018, air pollution values measured at Miskolc stations exceeded the daily concentration limit more than 35 occasions *(Table 3)*. In the most cases there are limit exceedances during the heating season in winter, which can be explained by the emission of solid-fired equipment [20].

Figure 2
The annual average values of air pollutants in Miskolc [µg/m³] [17], [18], [19]

Table 3
*Number of daily limit exceedances in Miskolc 2014–2018* [21]

Pollutant	Location	Number of daily limit exceedances [db]				
		2014	**2015**	**2016**	**2017**	**2018**
PM10	Miskolc, Alföldi Street	10	19	55	68	63
	Miskolc, Búza Square	61	55	40	68	84
	Miskolc, Lavotta Street	59	40	40	42	32

## 2. THE RELATIONSHIP BETWEEN RESIDENTIAL SOLID COMBUSTION AND THE REGIONS

In Hungary in 2011, slightly more than 45% of households used boilers, while 37% of households have been heated by convectors or stoves *(Figure 3)*. Heating types can be further grouped according to their fuel.

In the case of boiler and convector/stove heating type, if we rank the fuels according to the frequency of their use, the gas heating is in the first place, a second most common type of heating is mixed with gas and wood, and the only wood-firing is in the third place [22].

There is a strong correlation between residential solid fuel heating and regional development levels. Out of 174 districts, more than three-quarters of households in one of the district and more than half of households in 19 districts are exclusively heated with wood and in 22 districts more than three-quarters of households are heated (at least partially) with wood *(Figure 4)* [23].
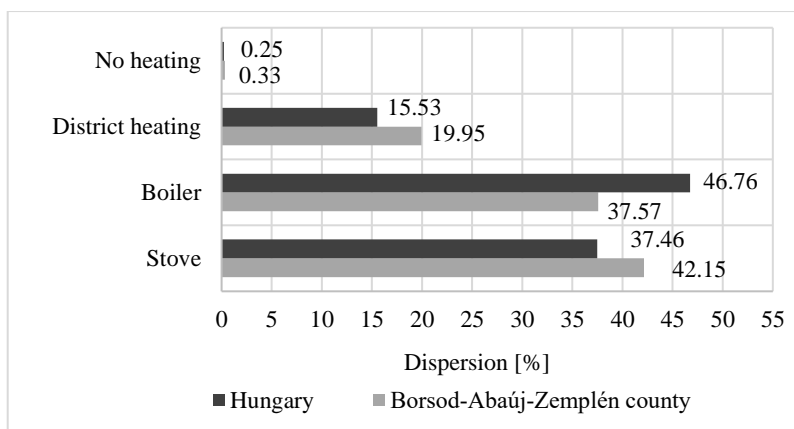
Figure 3
Distribution of households by type of heating in 2011 [22]
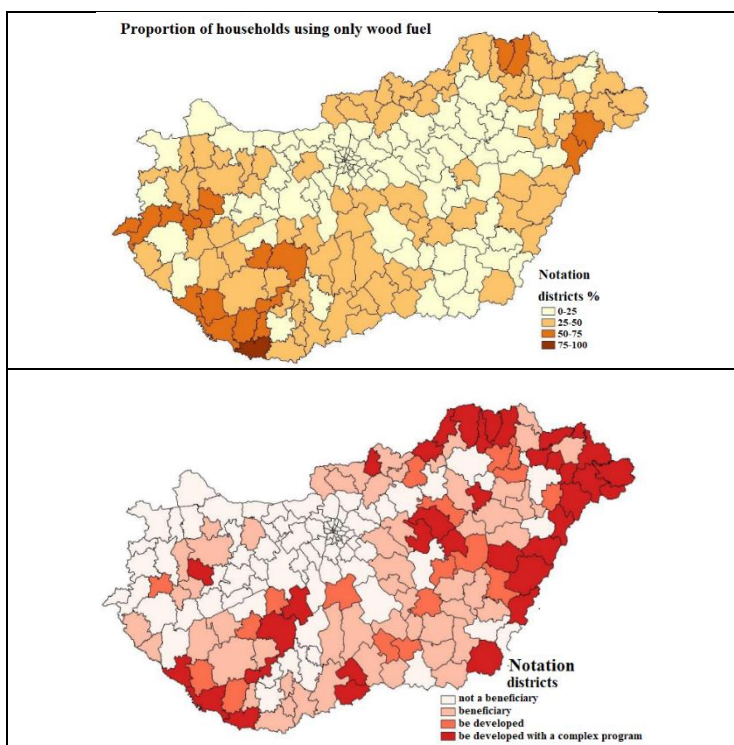
Figure 4
*In Hungary, the ratio of households using solid fuel (upper),
beneficiary regions classified by the 290/2014. (XI. 26.) Government
Decree (lower)* [23]

The complex indicator measuring the level of development of districts takes into consideration both socioeconomic and infrastructure development. Comparing the map showing the concentration of households which are heating with wood, with a map of complex indicators measuring the level of infrastructure development, it can be seen that among the 19 districts where more than 50 percent of the households are heated with wood, it is among the 11 most disadvantaged districts. Thus, the proportion of households heating with wood in disadvantaged districts is higher [23].

3. EMISSIONS FROM RESIDENTIAL HEATING, THE NEW RESTRICTION

While emissions from industry can be measured and limited, the control of citizens mixed-fired equipment is difficult. Authorities are not able to act against illegal burning, arguing that there is no device in their hands to deal with the situation. As a result, the European Commission has issued the implementation of Commission Regulation (EU) 2015/1188 implementing Directive 2009/125/EC of the European Parliament and of the Council with regard to ecodesign requirements for local space heaters. According to the expectations with this limitation, the number of emissions from households will be decreased and it will become much more controllable. However, households that have old types of firing equipment are typically financially incapable of being buying a new one. Separate room heating systems operating with solid fuel from 1 January 2022 must meet the requirements of the following table *(Table 4)*, which include limit values for seasonal room heating efficiency and pollutant emissions.

Table 4

Limit values for the environmentally conscious design of solid fuel installations
[24]

	Efficiency (min) [%]	Emission of pollutants (max)			
		PM [mg/m³]	Gaseous organic compounds [mg/m³]	CO [mg/m³]	NOₓ [mg/m³]
open combustion solid fired individual room heating equipment	30	50	120	2,000	200
working with solid fuel (which different from pellet) individual room heating equipment with a closed combustion chamber	65	40	120	1,500	200
working with pellet individual room heating equipment with a closed combustion chamber	79	20	60	300	200

The European Environment Agency's 2016 guidebook summarized the emission values in case of different fuel *(Table 5)* and the amount of pollutants emitted by different combustion plants in case of wood firing *(Table 6)*. The values in the table are converted from GJ/g to mg/m^3. The air pollutants in the tables are emitted into the atmosphere during optimum operation of the combustion plants.

Table 5

The emission factor of stove [16]

Fuel	Pollutant				
	PM [mg/m^3]	NOx [mg/m^3]	Benzo[a]pyrene [µg/m^3]	CO [mg/m^3]	SO$_x$ [mg/m^3]
Firewood	73.87	2.46	5.96	196.99	0.54
Lignite	37.51	4.17	10.42	208.39	37.51
Coal	18.52	6.04	6.04	80.53	18.12

One of the biggest advantage of wood against coal is that it contains just a little amount of sulfur or not at all. Therefore, the resulting SO$_x$ emissions will also be significantly lower. In terms of unit energy, the emission of the particulate matters is the highest during wood burning.

Table 6

Emission factors of different combustion plants in case of wood firing [16]

Equipment	Pollutant				
	PM [mg/m^3]	NOx [mg/m^3]	Benzo[a]pyrene [µg/m^3]	CO [mg/m^3]	SO$_x$ [mg/m^3]
Open fireplace	81.75	2.46	5.96	196.99	0.54
Traditional stove	73.87	2.46	5.96	196.99	0.54
Traditional boiler	46.79	3.94	5.96	196.99	0.54
Energy saving stove	36.94	3.94	5.96	196.99	0.54
Modern/Eco-labeled boiler	9.26	4.68	0.49	98.50	0.54
Pellet boiler	5.91	3.94	0.49	14.77	0.54

In *Table 6*, the fuel is the same in every case and the types of combustion equipments are varied. *Table 6* shows that the use of more modern technologies can significantly reduce emissions of both particulate matter and benzo[a]pyrene.

In the literature there are a lot of information about which parameters in the firing process can cause to the formation of air pollutants *(Table 7)*. Increased emissions of CO were found at high excess air ratios. This is probably a result of the cooling of the combustion process. The enhanced emissions of CO were accompanied by emissions of other unoxidized components: total organic carbon, and polycyclic aromatic hydrocarbons [25], [27]. To maximize combustion efficiency and minimize PAH emissions, the fuel moisture content should be low [29].

The mass concentration of particles was larger in the worst old-type case. From the number and mass size distributions, it can be concluded that the emission of sub-micron particles is enhanced by poorer combustion conditions [25]. The high ash content of the fuel leads to the formation of more particulate matter [30].

It was also observed, that during the firing phase and after fuel adding PM size distribution changed slightly to bigger size fraction. This is probably caused by an insufficient supply of air and insufficient mixing of air and fuel [26].

CO and particulate emissions composition are mainly influenced by fuel such as the households waste and the wood type, i.e. structure, elemental composition, water or ash content[26], [28].

Table 7

Effect of firing parameters on emission factors

Characteristics of the equipment	Fuel	Moisture content [m/m %]	PM [mg/m³]	NOx [mg/m³]	PAH [mg/m³]	CO [mg/m³]
Old type boiler [25]	firewood	15	17.24	3.55	n/a	256.09
	firewood	15	108.35	1.38	3.15	807.67
Modern type boiler [25]	firewood	15	1.33	6.16	0.01	34.82
	firewood	26	1.21	5.37	0.01	24.53
	firewood	38	4.18	4.75	0.14	177.77
Old type tile stove [26]	Alder and MSW	14–18	160.34	386.20	0.87 *µg/m³	4,640
11 kW Pellet stove [27]	firewood	7.9	n/a	6.83	0.02	1,288.80
	firewood-household waste	8.5	n/a	14.73	0.08	1,098.26
	demolition and construction wood waste-household waste	4.6	n/a	90.36	0.02	339.85
Logwood stove 6 kW (primary and secondary air) [28]	briquette standard test	7.7	150.9	176	n/a	1,331
	beech standard test	6.5	111.4	155	n/a	2,779
	oak standard test	9.7	107.3	166	n/a	2,948
	spruce standard test	8.5	156.6	96	n/a	2,240
	spruce standard test	8.5	124.2	87	n/a	2,161
	spruce low air	8.5	312	86	n/a	2,841
	spruce high fuel	8.5	118	80	n/a	1,989

CONCLUSION

Most of European population live in a place – mainly in cities – where the air pollution exceeds the air quality limits at certain regular intervals: the NO_2 and particulate matter pollution pose a serious health risk.

The biggest emitters of air pollutants are the industry, the agriculture, the transport and the households. Regardless of the quality of the combustion process, solid powder and polycyclic aromatic compounds are formed during solid firing in the household. The quality of combustion is strongly influenced by the quality of the fuel used, the type and age of the equipment, and the user's knowledge of the use of the equipment. As soon as the quality of the firing deteriorates due to any parameter, the number of air pollutants emitted into the atmosphere also increases.

This is exacerbated by the fact that in most cases, households with solid combustion plants (albeit illegal, though) are also burning household waste. There is not a proper way for authorities to clearly demonstrate the combustion of waste from flue gas and residual ash yet, therefore authorities are not able to act effectively against it. As a result, the European Commission has issued the implementation of Commission Regulation (EU) 2015/1188 implementing Directive 2009/125/EC of the European Parliament and of the Council with regard to ecodesign requirements for local space heaters.

Emissions would be reduced not only by modernizing the equipment but also by calling for the correct use of combustion equipment and by developing the flue gas cleaning equipment for residential use.

A further direction of the research is to find a connection between the amount of gas and solid air pollutants in the flue gas, the components remaining in the ash and the fuel used. Hopefully, with the help of the connection found, it would be easier to detect illegal waste combustion.

REFERENCES

[1] Uramné Lantai Katalin (2016). *PM10 szilárd részecskék forrás-hozzárendelése és a szmoghelyzet elemzése az Országos Légszennyezettségi Mérőhálózat adatai alapján*. Miskolci Egyetem, Miskolc.

[2] Európai Számvevőszék (2018). *Légszennyezés: egészségünk védelme még mindig nem elégséges.* [Online] Available: https://www.eca.europa.eu/Lists/ECA-Documents/SR18_23/SR_AIR_QUALITY_HU.pdf, accessed: 08-May-2019.

[3]   European Commission (2018). *Communication from the Commission to the European Parliament, the Council, the European Economic and Social Committee and the Committee of the Regions a Europe that protects: Clean air for all.* Brussels.

[4]   Mentes, D. (2018). *A génállomány megduplázásának hatása az energiafűz tüzelhetőségi feltételeire.* Miskolci Egyetem, diplomamunka.

[5]   Bozó L., Györgyné Váraljai I., Ivanics I., Vaskövi B. (2001). *A környezeti levegszennyezettség mérésének gyakorlata. Kézikönyv az immisszió vizsgálatához.* Budapest.

[6]   4/2011. (I. 14.) VM rendelet a levegőterheltségi szint határértékeiről és a helyhez kötött légszennyező pontforrások kibocsátási határértékeiről. *Hatályos Jogszabályok Gyűjteménye.* [Online] Available: https://net.jogtar. hu/jogszabaly?docid=a1100004.vm, accessed: 08-Apr-2019.

[7]   Nisbet, I. C. T., LaGoy, P. K. (1992). Toxic equivalency factors (TEFs) for polycyclic aromatic hydrocarbons (PAHs). *Regul. Toxicol. Pharmacol.*, vol. 16, no. 3, pp. 290–300.

[8]   Mukai, M., Thomas, J. F., Tebbens, B. D. (1968). Fate of airborne benzo[a]pyrene. *Environ. Sci. Technol.*, vol. 2, no. 1, pp. 33–39.

[9]   Butler, J. D., Crossley, P. (1981). Reactivity of polycyclic aromatic hydrocarbons adsorbed on soot particles. *Atmos. Environ.*, vol. 15, no. 1, pp. 91–94.

[10] *STADAT – 5.3.3. Nemzetgazdasági ágak szén-dioxid (CO_2) kibocsátása (1985–).* [Online] Available: https://www.ksh.hu/docs/hun/xstadat/xstadat_eves/i_ua026d.html, accessed: 08-Apr-2019.

[11] *STADAT – 5.3.1. Légszennyező anyagok és üvegházhatású gázok kibocsátása (1985–).* [Online] Available: https://www.ksh.hu/docs/hun/xstadat/xstadat_eves/i_ua002d.html, accessed: 08-Apr-2019.

[12] *STADAT – 5.3.12. Nemzetgazdasági ágak nitrogén-oxidok (NO_X) kibocsátása (1990–).* [Online] Available: https://www.ksh.hu/docs/hun/xstadat/xstadat_eves/i_ua031d.html, accessed: 31-Jul-2019.

[13] *STADAT – 5.3.17. Nemzetgazdasági ágak szén-monoxid (CO) kibocsátása (1990–).* [Online] Available: https://www.ksh.hu/docs/hun/xstadat/xstadat_eves/i_ua035d.html, accessed: 31-Jul-2019.

[14] *STADAT – 5.3.19. Nemzetgazdasági ágak 2,5 µm átmérő alatti szálló por ($PM_{2,5}$) kibocsátása (2000–).* [Online] Available: https://www.ksh.hu/docs/hun/xstadat/xstadat_eves/i_ua040b.html, accessed: 31-Jul-2019.

[15] *STADAT – 5.3.18. Nemzetgazdasági ágak 10 μm átmérő alatti szálló por (PM$_{10}$) kibocsátása (2000–)*. [Online] Available: https://www.ksh.hu/docs/hun/xstada t/xstadat_eves/i_ua036b.html, accessed: 31-Jul-2019.

[16] ÉLFO LRK Adatközpont (2018). 2*017. évi összesítő értékelés hazánk leveg-őminőségéről az automata mérőhálózat adatai alapján*.

[17] *STADAT – 5.3.27. A levegő szén-monoxid (CO)-szennyezettsége az automata mérőhálózat adatai alapján (2003–)*. [Online] Available: https://www.ksh.hu /docs/hun/xstadat/xstadat_eves/i_ua011c.html, accessed: 08-Apr-2019.

[18] *STADAT – 5.3.24. A levegő nitrogén-dioxid (NO$_2$)-szennyezettsége az automata mérőhálózat adatai alapján (2003–)*. [Online] Available: https://www.ksh.hu/docs/hun/xstadat/xstadat_eves/i_ua007c.html, accessed: 08-Apr-2019.

[19] *STADAT – 5.3.28. A levegő 10 μm átmérő alatti szálló porral (PM$_{10}$) való szennyezettsége az automata mérőhálózat adatai alapján (2003–)*. [Online]. Available: https://www.ksh.hu/docs/hun/xstadat/xstadat_eves/i_ua008c. html. accesse d: 08-Apr-2019.

[20] Lantai K. (2013). Levegőminőség vizsgálata, szmoghelyzetek elemzése az Észak-Magyarország régióban. *Anyagmérnöki Tudományok*, vol. 38, no. 1, pp. 309–318.

[21] *OLM – Automata mérőhálózat*. [Online] Available: http://www.levego mino seg.hu/automata-merohalozat?city=15, accessed: 08-Apr-2019.

[22] *Központi Statisztikai Hivatal-Népszámlálási Adatok 2011*. [Online]. Available: http://www.ksh.hu/nepszamlalas/tablak_teruleti_00, accessed: 08-Apr-2019.

[23] Bajomi A. Zs. (2018). *A szociális tüzelőanyag-támogatás Magyarországon*. [Online] Available: https://habitat.hu/wp-content/uploads/2018/09/hfhh_tuzifa_tanul many.pdf, accessed: 08-Apr-2019.

[24] The European Comission (2015). Implementing Directive 2009/125/EC of the European Parliament and of the Council with regard to ecodesign requirements for solid fuel local space heaters. *Off. J. Eur. Union*, no. 5, pp. 1–19.

[25] Johansson, L. S., Leckner, B., Gustavsson, L., Cooper, D., Tullin, C., Potter, A. (2004). Emission characteristics of modern and old-type residential boilers fired with wood logs and wood pellets. *Atmos. Environ.*, vol. 38, no. 25, pp. 4183–4195.

[26] Maasikmets, M., Kupri, H.-L., Teinemaa, E., Vainumae, K., Arumae, T., Roots, O., Kimmel, V. (2016). Emissions from burning municipal solid waste and wood in domestic heaters. *Atmos. Pollut. Res.*, vol. 7, no. 3, pp. 438–446.

[27] Edo, M., Ortuño, N., Persson, P.-E., Conesa, J. A., Jansson, S. (2018). Emissions of toxic pollutants from co-combustion of demolition and

construction wood and household waste fuel blends. *Chemosphere*, vol. 203, pp. 506–513.

[28]   Schmidl, C., Luisser, M., Padouvas, E., Lasselsberger, L., Rzaca, M., Ramirez-Santa Cruz, C., Handler, M., Peng, G., Bauer, H., Puxbaum, H. (2011). Particulate and gaseous emissions from manually and automatically fired small scale combustion systems. *Atmos. Environ.*, vol. 45, pp. 7443–7454.

[29]   Bignal, K. L., Langridge, S., Zhou, J. L. (2008). Release of polycyclic aromatic hydrocarbons, carbon monoxide and particulate matter from biomass combustion in a wood-fired boiler under varying boiler conditions. *Atmos. Environ.*, vol. 42, no. 39, pp. 8863–8871.

[30]   Obaidullah, M., Bram, S., Verma, V. K., De Ruyck, J. (2012). A Review on Particle Emissions from Small Scale Biomass Combustion. *Int. J. Renew. Energy Res.*, vol. 2, no. 1, pp. 147–159.

THE FIRING PROPERTIES OF THE BIOFRACTION AND RDF PELLETS

DÓRA MENTES[1]–EMESE SEBE[2]–ANDRÁS A. KÁLLAY[3]–CSABA PÓLISKA[4]

Many cities in developing countries are facing serious problems in dealing with huge municipal solid waste (MSW) generated. The energy recovery of accumulated municipal waste can provide an alternative to replacing a small part of fossil fuels. Refuse Derived Fuel (RDF) is a secondary fuel that contains higher-calorific components of communal waste. The quality of pellets made from RDF and their combustion properties can be influenced by a number of factors. The combustion properties must be known in the interest of forecast the behavior of the fuel during the combustion.

Keywords: combustion parameters of RDF, physical composition of RDF

INTRODUCTION

Increased demand for renewable energy sources, high organic matter content of municipal solid waste, and a limited number of landfill sites make the use of municipal solid waste as a source of energy, biochemical and thermochemical more and more popular [1], [2], [3]. Municipal solid waste (MSW) is a poor-quality fuel and its pre-processing is necessary to prepare fuel pellets to improve its consistency, storage and handling characteristics, combustion behavior and calorific value [4].

Generally speaking, sewage sludge, waste wood, high calorific fractions from mechanical-physical (MPT) and/or mechanical–biological treatment (MBT) plants, calorific fractions of household and commercial waste, shredder lightweight fractions (e.g., electrical and electronic equipment), scrap tyres, food by-products (fats, animal meal, etc.) waste oil, used solvents and viscose plant off gas, etc. may be considered as "Refuse Derived Fuel" (RDF). In the narrow sense of the definition, solid fuels which are prepared from sorted or mixed solid wastes (municipal waste fractions, commercial wastes, production wastes, lightweight fractions from MBT/MPT-plants, etc.) are described as "Solid Recovered Fuel" (SRF) [5]. This fuel

[1] Department of Combustion Technology and Thermal Energy, University of Miskolc
H-3515 Miskolc-Egyetemváros, Hungary
tuzdora@uni-miskolc.hu

[2] Department of Combustion Technology and Thermal Energy, University of Miskolc
H-3515 Miskolc-Egyetemváros, Hungary
emesesebe@gmail.com

[3] Department of Combustion Technology and Thermal Energy, University of Miskolc
H-3515 Miskolc-Egyetemváros, Hungary
tuzaak@uni-miskolc.hu

[4] Department of Combustion Technology and Thermal Energy, University of Miskolc
H-3515 Miskolc-Egyetemváros, Hungary
tuzcsaba@uni-miskolc.hu

is a special type of solid municipal waste that contains only a small percentage of non-combustible materials such as metal and glass [6].

Refuse-derived fuels (RDF) are used in power plants, material industry, mono combustion facilities and co-firing plants. It is known from operating experience – concerning the energy conversion density, the ignition and burnout behavior, the slag formation and corrosion potential – and from comparing the combustion behavior with fossil fuels, that biomass fuels and RDF can be seen as difficult fuels [7].

The production of RDF (or SRF) pellets, which is the subject of our investigation, consists of several single operations to separate unwanted as well as combustible components to achieve optimal combustion parameters. The main operations are filtering; crushing; size reduction; classification: separation of metal, glass or wet organic matter; drying; compression [4].

For higher qualities of RDF and/or SRF, a multi-stage separation process is necessary for manufacturing, including the unit operations of classifying and sorting of waste material fractions, as well as the separation of ferrous and non-ferrous metals and also unwanted heavyweight inert materials (e.g. stones, glass, ceramics, etc.) followed by confectioning of the fuel according to specifications given. The final quality of RDF (or SRF) will ultimately depend on the composition of the input (feeding) materials, as well as on the extent and the intensity of the applied recovery process *(Figure 1)* [5].
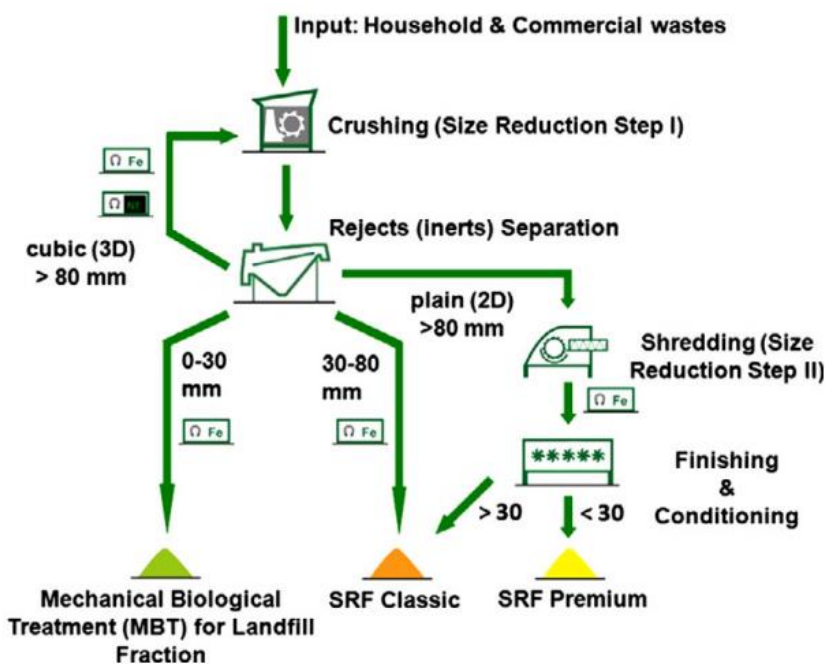

Figure 1
Simplified processing scheme for different RDF/SRF specifications [5]

The physical composition of the RDF pellets found in the literature is shown in *Table 1*, while *Table 2* includes the combustion properties.

Table 1

The physical composition of RDF pellets

Ref.	Plastic	Paper carton	Textile	Biomass	Composite	Food waste	Fine fraction	Other	HHV*
	% m/m								MJ/kg
[1]	17.3	57.1	*	4	–	18.6	–	3.2	19.4 dry
[5]	16	6	5	6	3	–	55	9	n/a
[7]	4	21	*	41	4	–	20	10	8 wet
[8]	23	35.1	14	2.1	–	–	20.3	5.5	16.5 dry
[8]	20	25	0	15	–	–	–	40	17.2 dry
[8]	9	55	5	0	–	–	–	31	17.4 dry
[9]	41.5	3.4	21.3	16.7	–	–	10.4	6.8	15.6 wet
[9]	54.9	3.0	14.2	18.5	–	–	0.8	8.7	16.5 wet
[9]	64.5	0.6	11.4	9.9	–	–	1.0	12.6	19.3 wet
[10]	24.5	27.9	8.7	5.9	–	–	23.2	9.3	23.4 dry
[11]	14.4	14.3	59.4	2.1	4.7	–	–	5.1	21.7 dry
[12]	42.1	42.1	41.2	7.0	9.6	–	–	–	23.7 wet
[12]	24.0	24.0	23.5	4.0	48.5	–	–	–	16.1 wet
[12]	24.0	24.0	23.5	4.0	25	–	–	23.5	17.6 wet

* HHV – higher heating value
highlighted area – LHV lower heating value
n/a. – no available

The visual inspection of the fine fraction showed that it is a heterogeneous material dominated by soil-like materials and minerals and also contain different quantities of landfilled materials [13]. Fine fractions can be considered as a relevant source of metals and calorific fractions, as well as a fraction suitable for inert and soil-like material recovery [14].

Other types of waste include glass, metal, hazardous household waste, inert waste, health-care waste, various combustible and non-combustible.

In contrast, the carbon content and calorific value were increased by increasing organic waste content up to 40% of the total weight of RDF. The similar trend has been seen for hydrogen content, but it was in lower magnitude. The oxygen content was shown on the opposite response to the carbon content and calorific value, while the nitrogen content tends to increase by putting more organic waste [15].

As shown in *Table 1* the heating value of RDF pellets may differ depending on their composition. The composition of municipal solid waste varies from day to day, so the properties of RDF pellets will also be different [7].

Combustion properties of RDF pellets (dry-basis)

Ref.	Moisture	Ash	N	C	H	S	O	HHV
	% m/m							MJ/kg
[9]	17.60	40.00	0.95	35.95	4.50	0.45	n/a	15.60
[9]	19.55	32.30	1.25	44.80	7.15	0.45	n/a	16.50
[9]	19.35	36.05	1.25	43.45	5.90	0.39	n/a	19.25
[16]	1.20	13.34	0.66	51.66	8.82	0.08	25.42	n/a
[17]	22.07	17.11	0.94	45.09	5.78	0.15	30.94	23.44
[18]	n/a	14.70	0.77	43.92	6.36	0.29	33.48	19.54
[18]	n/a	23.75	1.20	47.40	6.15	0.22	19.78	22.55
[15]	6.40	9.20	10.77	49.75	9.04	1.89	28.55	24.96

n/a – no available

According to the literature, the moisture content of RDF pellets can vary ranges from 1.2% m/m to 22.07% m/m, ash content from 9.2% m/m to 40% m/m, and heating value from 15.6 MJ/kg to 24.96 MJ/kg *(Table 2)*.

The RDF pellets studied in this article are utilized by pyrolysis. Pyrolysis is nothing more than thermal decomposition in an oxygen-free medium. During the thermal decomposition, gas, liquid and solid end products are formed. The number of end products can vary over a wide range depending on the parameters of the experiment; from pyrolysis temperature, heating rate, pyrolysis time, etc. [19].

It is important to know the combustion parameters of all materials used for energy purposes. In the course of the research, the combustion properties of the RDF pellets and the ash content of the char left behind from pyrolysis were examined.

1. MATERIALS AND METHODS

The investigated RDF pellets were manufactured from solid municipal solid waste, so there is no information on the actual composition of the pellets. The two types of RDF pellets were produced with a difference of about 20 days. Biofraction pellets are manufactured from the bottom product (containing a large amount of organic matter) by selecting municipal solid waste with trommel. The blend pellet contains 34% m/m of RDF pellet and 66% m/m of biofraction.

Organic substances are mostly found in the particle size fraction below 50 mm so that biofraction containing mostly organic matter can be produced from the residual waste with grading and other separation processes. This fraction is very different from the selectively collected green waste, its composition is much more heterogeneous. In addition at the side of biodegradable many other types of waste are presented, such as hazardous waste, because the people cannot be motivated to collect waste responsibly.

The pellets were subjected to the following combustion tests:

- Determination of the moisture content of pellets happens in a drying oven at 105 ± 5 °C by mass content, according to MSZ EN 14774:2010 standard.
- Determination of ash content of pellets and char from pyrolysis by heating to 550 ± 15 °C to constant mass according to MSZ EN 14775: 2010.
- Carlo Erba EA1108 type ultimate analyzer was used for the measurement of the C-, H-, N-, S-, O-content in the pellets according to MSZ EN 15104:2011 standard.
- The calorific test was performed using a Parr 6200 type isoperibol oxygen bomb calorimeter according to MSZ EN 14918:2010 standard. The lower heating value is calculated from the higher heating value, the hydrogen content and the moisture content.
- Determination of the softening and sintering temperature of ash from combustion using a SYLAB IF2000G type heating microscope.
- Thermoanalytical analysis with MOM Q1500D type derivatograph.

The pyrolysis of RDF pellets occurred at 600 °C with a heating rate of 60 °C/h. After the experiments, the solid product (char) was also tested.

2. COMBUSTION PROPERTIES OF PELLETS

Table 3 shows the combustion properties of the samples. The table also contains the parameters of a good quality wood pellet as a reference value.

Table 3

Combustion properties of pellets tested (dry-basis)

Sample	Moisture	Ash	N	C	H	S	O	HHV*
	% m/m							MJ/kg
1. RDF pellet	4.20	17.02	1.33	49.44	6.44	0.42	25.35	22.42
2. RDP pellet	4.74	19.98	1.37	44.22	5.57	0.18	28.67	20.93
Biofraction	4.04	56.68	1.59	24.09	2.84	0.51	14.28	9.07
Blend pellet	4.32	41.16	1.33	38.16	4.88	0.17	14.31	14.83
Wood pellet	7.70	0.79	0.22	44.59	6.11	0.05	48.59	18.24

*HHV– higher calorific value

Although the composition of the pellets tested differs, the hygroscopic moisture content is almost the same. The ash content of RDF pellets is relatively high. This is partly due to the fact that the municipal solid waste, despite the selection, still contains non-combustible materials that go through the system and have not decomposed during keeping the heat at 550 °C. Another possible reason is that during the manufacture of some plastics (like gum), fillers were used that are also non-combustible.

Based on the information in the literature, RDF pellet samples may contain high carbon content material due to the heating value around 20 MJ/kg.

As regards the comparison of RDF pellet 1 and wood pellet, the much higher heat value of the RDF pellet is due to the higher carbon content and lower moisture content. At the same time, the ash content and nitrogen content are higher, which can be considered unfavorable in the case of combustion.

Table 4 shows the proximate analysis of the pellets. As we can see, there is a strong relationship between the fix carbon content of the samples and the heating value. The RDF pellet 1 sample has the highest fix carbon content and the highest calorific value.

Table 4

Proximate analysis of pellets tested

Sample	Moisture	Volatile	Fix carbon	Ash
	% m/m			
1. RDF pellet	11.02	41.07	30.40	17.51
2. RDF pellet	8.51	45.09	24.25	22.15
Biofraction	22.08	23.73	12.19	42.00
Blend pellet	13.94	39.41	28.12	18.50
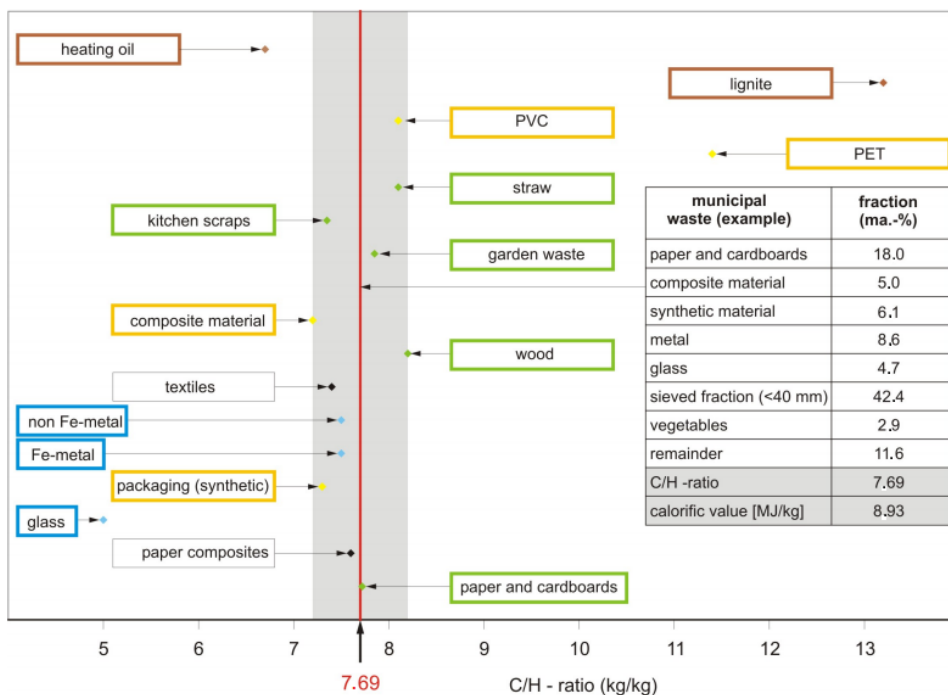
Figure 2

Illustration of the C/H ratio of different material groups in comparison to municipal waste set as an example [7]

Figure 2 shows for the single material groups, that the C/H ratio lies within a range between 7 and 8. A relative enrichment with synthetic material (exceptional for PET) in comparison to biogenic material groups, for e.g. household waste, paper/cardboard, there is no significant change in the C/H ratio. However, an increase in the C/O ratio with rising C-content is a resultant noticed *(Figure 3)* [7].
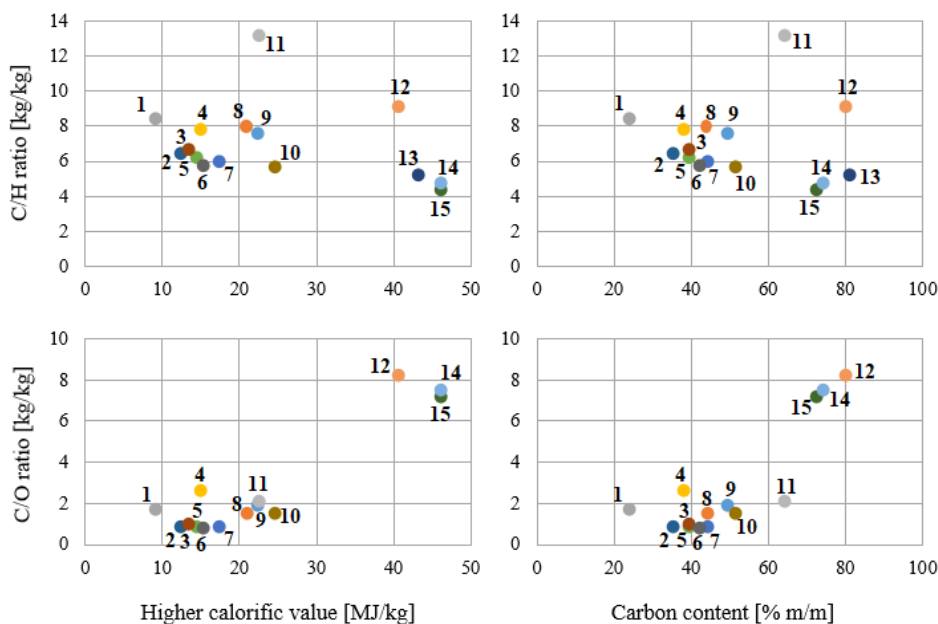
Figure 3

C/H and C/O ratios plotted against the higher calorific value and the carbon content for different waste fractions and different refuse-derived fuels

1. Biofraction
2. Glossy paper
3. Recycled newsprint
4. RDF/Bio mix
5. Carton
6. Paper napkin
7. Textil
8. 2. RDF
9. 1. RDF
10. 84C/PAP (e.g., juice box)
11. PET
12. PS (e.g., sourcream box)
13. 90 C/PP (e.g., bag of chips)
14. HDPE 1.
15. HDPE 2.

According to *Figure 3*, the RDF/Bio mixture is located near the group of paper and textiles, while the group of plastics is severely separated. From this consideration it can be derived, that refuse-derived fuels with increasing calorific value the C/H ratio approximately remains constant and the C/O ratio, however, increases *(Figure 3)* [7]. If the physical composition of the RDF sample is not known, we can get a good approximation from the investigation of the C/O ratio, the C/H ratio, the calorific value, and the carbon content. *Figure 3* illustrates well that which materials can be in the RDF.

3. INVESTIGATION OF SOLID BY-PRODUCTS AFTER COMBUSTION AND PYROLYSIS OF RDF PELLETS

RDF pellets can be utilized on a large scale in many ways. One possibility is to operate a heat generating device with RDF fuel and the other to use it as a pyrolysis feedstock. In the latter case, the ultimate goal is to maximize the amount of gaseous product. In either case, there are solid by-products of RDF pellets remaining after combustion and pyrolysis, called ash and char. The investigation results of these solid residues are shown below.

3.1. Determination of softening parameters of RDF ash

Attention should be paid to solving the problem of slag formation and corrosion caused by it when the RDF pellets are used in high-temperature operation. The degree of damage to the combustion plant is influenced by the chemical and mineral composition of the ash resulting from the combustion, the sintering, softening and melting properties [20]. In-laboratory softening studies indicate with acceptable accuracy the behavior of ash in industrial boilers (amount of ash deposited in the combustion chamber and heat exchanger surfaces, ash aggregation, and corrosion caused by it) [21].
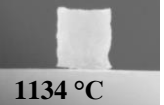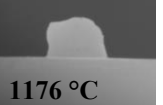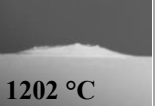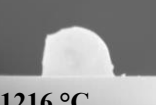
Sample	Temperature °C			
1. RDF pellet	501 °C	1134 °C	1176 °C	1202 °C
Biofraction pellet	501 °C	1125 °C	1216 °C	1486 °C

Figure 4

Images of ash from 1. RDF pellets and biofraction made during ash softening testing

Based on previous experiences [22], the biofraction could have contain several substances that increase the melting point temperature (Si, Ca, Mg, Al) of the resulting ash, while the 1. RDF pellet may contain alkali metal (Na, K) and phosphorus oxides because of its lower melting point. In both cases, the sphericalization of the ash samples starts at around 1,160 °C. This temperature is well above the temperature of the pyrolysis, so it cannot cause any problems.
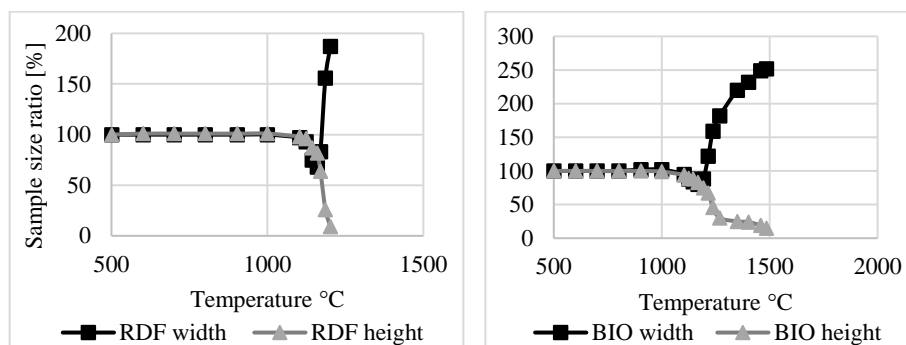
Figure 5
Degree of deformation of ash samples from 1. RDF pellets and biofraction

3.2. Determination of ash content of RDF char

The ash content of the char samples remaining after pyrolysis was also analyzed, the results of which are shown in *Table 5* below.

Table 5
Ash content of chars

Sample	Ash content % m/m
Char of RDF pellet pyrolyzed at 700 °C	53.25 ± 1.64
Char of biofraction pellet pyrolyzed at 700 °C	84.14 ± 0.17
Char of blend pellet pyrolyzed at 700 °C	77.24 ± 2.13

The ash content of pyrolyzed pellets under the same conditions may be different due to their composition. The higher the ash content of the pyrolyzed sample the less content of combustible in it. It can be stated that the settings for pyrolysis should be adapted to the composition of the RDF pellet. Thus, the organic composition of the waste not only influences the moisture and ash content of the fuel as well as the heat of combustion but also the setting of the parameters of pyrolysis.

Although, there is no effect on pyrolysis, the softening properties of ash of the char will be tested in the future.

CONCLUSION

The article examines the combustion properties important for the usability of RDF pellets: physical composition, moisture content, ash content, element composition, lower and higher heating value, ash softening and sintering properties. Refuse-derived fuels are used in power plants, material industry, mono combustion facilities and co-firing plants. RDF pellets can be utilized on a large scale in many ways. One

possibility is to operate a heat generating device with RDF fuel and the other to use it as a pyrolysis feedstock.

Several factors influence the combustion parameters of RDF pellets:

1. The great difference in combustion properties is due to the different composition of heterogeneous components of RDF pellets (such as wood, fabric, plastic), which is caused by the ever-changing composition of municipal solid waste due to different consuming habits of people. This is a relatively poor-quality fuel and its pre-processing is necessary to prepare fuel pellets to improve its consistency, storage and handling characteristics, combustion behavior and calorific value. However, recycling of this waste is necessary, and pyrolysis could represent a solution.

2. In manufacturing technology, as there are no standards for the production of RDF (unlike for the production of SRF), there may be significant differences between the quality of RDF from different producers.

The different ash content of chars is also due to the different proportions of the components found in RDF pellets. It can be stated that the settings for pyrolysis should be adapted to the composition of the RDF pellet. Thus, the organic composition of the waste not only influences the moisture and ash content of the fuel as well as the heat of combustion but also the setting of the parameters of pyrolysis.

REFERENCES

[1] Suzuki, T., Tsuruda, T., Ogawa, Y., Liao, C. (2005). A Study on Extinction of RDF (Refuse Derived Fuel) Pile. *Fire Safety Science,* vol. 8, pp. 789–800.

[2] Efika, E. C., Onwudili, J. A., Williams, P. T. (2015). Products from the high temperature pyrolysis of RDF at slow and rapid heating rates. *J. Anal. Appl. Pyrolysis*, vol. 112, pp. 14–22.

[3] Sprenger, C. J., Tabil, L. G., Soleimani, M., Agnew, J., Harrison, A. (2018). Pelletization of Refuse-Derived Fuel Fluff to Produce High Quality Feedstock. *J. Energy Resour. Technol.*, vol. 140, no. 4, p. 042003.

[4]   Zafar, S. Pelletization of Municipal Solid Wastes. *BioEnergy Consult*. [Online]. Available: https://www.bioenergyconsult.com/tag/rdf-pellets/, accessed: 14-May-2019.

[5]   Sarc R., Lorber, K. E. (2013). Production, quality and quality assurance of Refuse Derived Fuels (RDFs). *Waste Manag.*, vol. 33, no. 9, pp. 1825–1834.

[6]   Beckmann, S. N. M. (2007). Characterisation of Refuse Derived Fuels (RDF) in reference to the Fuel Technical Properties. In: *International Conference on Incineration and Thermal Treatment Technologies-IT3*, vol. 26, pp. 379–394.

[7]   Pohl, M. B. M., Gebauer, K. (2008). Characterisation of Refuse Derived Fuels in view of the Fuel Technical Properties. In: *INFUB – 8th European conference on industrial furnaces and boilers*, vol. 8, pp. 1–11.

[8]   Marsh, R., Griffiths, A. J., Williams, K. P., Wilcox, S. J. (2007). Physical and thermal properties of extruded refuse derived fuel. *Fuel Process. Technol.*, vol. 88, no. 7, pp. 701–706.

[9]   Rotheut, M., Quicker, P. (2017). Energetic utilisation of refuse derived fuels from landfill mining. *Waste Manag.*, vol. 62, pp. 101–117.

[10]   Montejo, C., Costa, C., Ramos, P., Márquez, M. del C. (2011). Analysis and comparison of municipal solid waste and reject fraction as fuels for incineration plants. *Appl. Therm. Eng.*, vol. 31, no. 13, pp. 2135–2140.

[11]   Vasconcelos, C., Silva, R. B., Martins-Dias, S. (2014). Insight on the self-ignition behaviour of RDF components. Lisboa, Portugal. [Online] Available: https://fenix.tecnico.ulisboa.pt/downloadFile/563345090413508/resumo.pdf, accessed: 14-May-2019.

[12]   Zhao, L., Giannis, A., Lam, W.-Y., Lin, S.-X., Yin, K., Yuan, G.-A., Wang, J.-Y. (2016). Characterization of Singapore RDF resources and analysis of their heating value. *Sustain. Environ. Res.*, vol. 26, no. 1, pp. 51–54.

[13]   Jani, Y., Kaczala, F., Marchand, C., Hogland, M., Kriipsalu, M., Hogland, W., Kihl, A. (2016). Characterisation of excavated fine fraction and waste composition from a Swedish landfill. *Waste Manag. Res.*, vol. 34, no. 12, pp. 1292–1299.

[14]   Parrodi, J. C. H., Höllen, D., Pomberger, R. (2018). Characterization of Fine Fractions From Landfill Mining: a Review of Previous Investigations. *Detritus*, vol. 2, no. 1, p. 46.

[15]   Dianda, P., Mahidin, Munawar, E. (2018). Production and characterization refuse derived fuel (RDF) from high organic and moisture contents of

municipal solid waste (MSW). *IOP Conf. Ser. Mater. Sci. Eng.*, vol. 334, no. 1, p. 012035.

[16] Haydary, J. (2016). Gasification of refuse-derived fuel (RDF). *Geosci. Eng.*, vol. 62, no. 1.

[17] Montejo, C., Costa, C., Ramos, P., Del, M., Marquez, C. (2011). Analysis and comparison of municipal solid waste and reject fraction as fuels for incineration plants. *Appl. Therm. Eng.* vol. 31, no. 13, pp. 2135–2150.

[18] Taylor, R., Chapman, C., Faraz, A. (2013). Transformations of syngas derived from landfilled wastes using the Gasplasma® process. In: *2nd International Enhanced Landfill Mining Symposium*. [Online] Available: http://www.app-uk.com/resources/uploads/TransformationsOfSyngasDerivedFromLand-filledWastesUsingGasplasma_ELFM2013.pdf, accessed: 15-May-2019.

[19] Czupy I. (2011) Mezőgazdasági (növénytermesztés, állattartás, erdészeti) hul-ladékok kezelése és hasznosítása. Digitális Tankönyvtár. *TAMOP 4.2.5 Pályázat könyvei*. [Online]. Available: https://www.tankonyvtar.hu/ hu/tarta-lom/tamop425/0021_Mezogazdasag_hulladekai/ch02.html, accessed: 16-May-2019.

[20] Woperáné dr. Serédi Ágnes, dr. Szemmelveisz Tamás, Koós Tamás, Baranyai Viktor Zsolt (2012). Biogáz adatbázis, Biomassza adatbázis, Szennyvíziszap adatbázis. Digitális Tankönyvtár. *TAMOP 4.2.5 Pályázat könyvei*. [Online]. Available: https://www.tankonyvtar.hu/hu/tartalom/tamop425/0001_1A_A2 _AB_ebook_biogaz_adatbazis_biomassza_adatbazis_szennyviziszap_adatba zis/adatok.html, accessed: 16-May-2019.

[21] Blas Melissari (2014). Ash related problems with high alkalii biomass and its mitigation - Experimental evaluation. *Mem. Investig. en Ing.*, vol. 12.

[22] Kelemenné Simándi A. (2016). *Kenderföldi Biomassza Fűtőmű hamujának vizsgálata és hasznosítási lehetőségei*. Miskolci Egyetem, Műszaki Anyag-tudományi Kar, diplomamunka.

# STUDY OF ELECTRODIALYTIC MATERIAL TRANSPORT AT THE ELECTROLYSIS OF AQUEOUS NaCl SOLUTIONS CONTAMINATED BY EPTC

FERENC MOGYORÓDY[1]

The electrolytic degradation of inorganic pollutants in pesticide wastewaters was studied in different electrodialysis systems. The experiments show us that nearby organic pollutant (EPTC) inorganic contamination (NaCl) is also degradable. The endproducts including SO_4^{2-} and NO_3^- are produced from the EPTC, and NaOH is produced from NaCl, in the known manner.

Keywords: electrodialysis, wastewater, degradation, thiocarbamate, inorganic pollutants

INTRODUCTION

Earlier it was reported on attempts to decompose thiolcarbamate type pesticides, including EPTC (1) in electrolysis of wastewater [1],

$$CH_3-CH_2-CH_2 \atop CH_3-CH_2-CH_2 \Big\rangle N-\overset{\overset{\text{O}}{\|}}{C}-S-CH_2-CH_3 \tag{1}$$
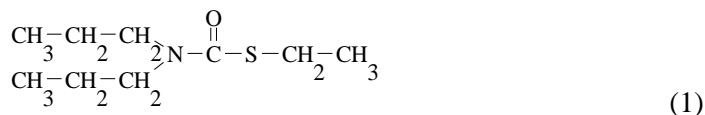
in a single undivided electrolysis cell *(Figure 1)* and partly in a two-cell electrolysis cell *(Figure 2)* where electrodialysis processes can also play a role.
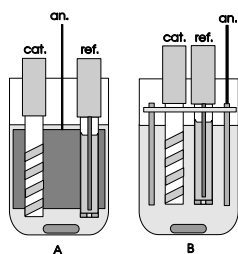

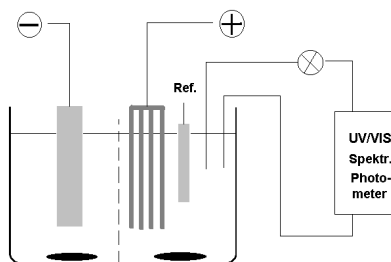***Figure 1***
Single-cell electrolysis equipment

Figure 2
Two-cell electrolysis equipment

---

[1]   Institute of Chemistry, University of Miskolc
       H-3515 Miskolc-Egyetemváros, Hungary
       fkmmf@uni-miskolc.hu

1. Materials and methods

Different structure electrodialysators were used in the laboratory experiments: the anode was DSA®, the cathode was a perforated sheet made of acid-resistant iron alloy, Ag/AgCl electrode was used as reference electrode. The constant potential was maintained by an EF 427 type potentiostate and a TR-9158 direct current source. The potentiostate was used in potentiometric mode in all our experiments and the current was registered.

The organic endproducts produced were analyzed by a Hewlett-Packard 1084B HPLC or a Chrompack Gas Chromatograph. Chlorine concentration and UV absorbance were measured with a Hewlett-Packard 8452A diode-array spectrophotometer. During the electrodialysis experiments pH was not measured, the produced NaOH was measured titrimetrically with HCl solution. The Cl^- concentration was determined titrimetrically with $AgNO_3$ solution. The SO_4^{2-} was determined gravimetrically by $BaCl_2$ precipitation and NO_3^- concentrations were determined photometrically by Na-salycilate method. COD measurements were made by standard bichromate measuring method.

Industrial filter fabric was used as diaphragm and also membranes (ion selective and bipolar membranes) i.e. NAFION (Du Pont products) with different codes were used.

Reagents
The initial concentration of the EPTC made by Sagrochem Ltd. was 100 ppm. The conducting electrolyte was $0.5\ kmol.m^{-3}$ NaCl (Reanal). The pH was set by HCl in the acid or by NaOH in the basic range. Distilled water was used as the solvent.

2. Results and discussion

Electrodialysis of NaCl and NaOH-containing EPTC solutions was first studied in a classical three-cell electrodialysis device known in the art *(Figure 3)*.
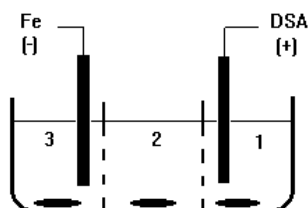

Figure 3
The classic three-cell electrodialysator

The device is made of polypropylene. The semi-permeable wall (diaphragm) was an industrial filter fabric through which clean water could not flow (without overpressure). Of the electrodes, the anode was DSA®, the cathode was stainless steel. In the cells, strong mixing was provided by magnetic stirrers. Each cells volume were about 15–20 ml. The surface of the electrodes was not determined exactly, the aim was the constant potential electrolysis. It worked visible. Due to the distance between the

electrodes and the diaphragms, the potential of 6.14 V, which is provided by the type of TR-9158 direct current source, the current was 0.6–0.7 A, and the change (decrease) shown in the figure 4 could be achieved by the initial solution (2) (Na$^+$) at the concentration of Cl$^-$ and NaOH, while the anolyte concentration of the anion in the anode space increased, the catholyte concentration of catholyte increased in the cathode space.
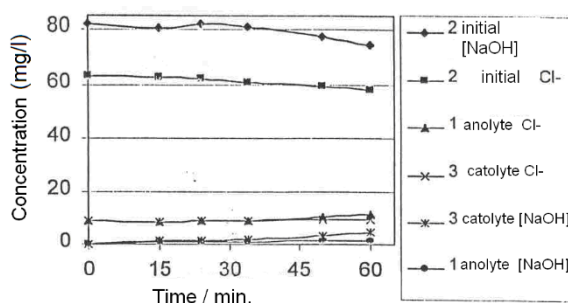

Figure 4
The electrolysis of 100 μl EPTC 10% NaCl, 10% NaOH
in classic three-cell electrodialysator

According to our UV spectrophotometric measurements, the EPTC concentration of the starting mixture, and more specifically the magnitude of the UV absorbance, did not change significantly. 100 ml of the starting mixture was extracted with 4 ml of CCl$_4$ and the UV absorbance was measured at 262 nm with a diode array spectrophotometer. Not in the catholyte, a barely detectable UV absorbance at 262 nm appeared in the anolyte, which means that EPTC transport in such an electrical dialysis is negligible but occurs as well as NaCl transport to the negligible cathode space and NaOH transport to the anode space.

Thus, in addition to electrodialysis, signs (effects) of diffusion in the traditional sense can be seen in the *Figure 4*.

In a two-cell device constructed from the same elements, but with a different design, at smaller cell voltages *(Figure 2)* we were able to achieve much greater changes in the composition of the starting NaCl and NaOH-containing EPTC solutions by the combination of electrodialysis and electrolysis. The electrolysis cell was the same volume as the three-cell electrodialysator but without the middle part. (Anode was DSA$^®$, cathode Fe, membrane: NAFION 324.) In these experiments, the EPTC concentration was measured by gas chromatography (Chrompack), NaOH, Cl$^-$, SO$_4^{2-}$, and NO$_3^-$ concentrations were determined as discribed earlier, chlorine concentration and UV absorbance were measured with a diode-array spectrophotometer.

Figure 5 shows that the rate of increase in NaOH concentration in the catholyte is significantly higher than in the 3-cell classical electrodialysis, so the transport of the Na$^+$-ion through the diaphragm is significant and the rate of increase in chlorine

UV absorbance is very fast in the anolyte until the saturation concentration is reached, chlorine is released from the system in gas form.
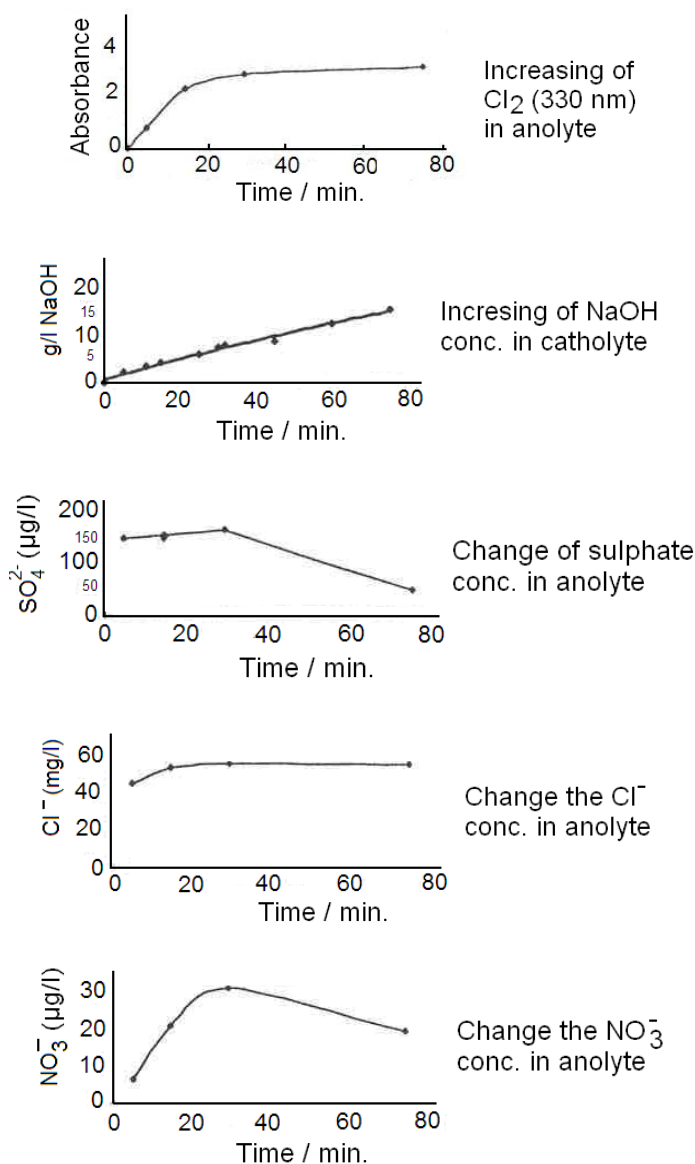

Figure 5
Diaphragm electrolysis – electrodialysis (200 μl EPTC/L 10% NaCl solution)
Pot.: 1.7 V, I = 4 A. Cl₂ – UV absorbance, the change of concentration of NaOH,
SO_4^{2-}, C^-, and NO_3^- in time

The strong Na^+-ion transport can also be deduced from the fact that the fluid level in the cathode space is always higher than in the anode space (due to the solvation of Na^+-ion, water also passes through the membrane and thus a significant osmotic pressure is generated). In the anolyte, the increase in Cl^--ion concentration – up to saturation concentration – provides the Cl^--ion supply for Cl_2 generation.

Thus, Cl^--ion transport from the cathode space continuously provides equilibrium Cl^- concentration around the anode. The change in the concentration of organic pollutant (EPTC) and the rate of decrease are not shown in the figure, this has already reported in detail [4].

Now it was only checked by the fact of rapid, complete decomposition by gas chromatography. EPTC, the organic pollution, disappeared completely from the anolyte.

From the EPTC in the anode space, as a result of degradation, nitrate and sulphate are also produced (this also indicates that not only the EPTC but also its degradation intermediates are degraded) and nitrate and sulphate are likely to be involved in further reactions – based on the nature of the curves (maximum curve).

Thus, our experiments with electrodialysis and electrolysis (diaphragm electrolysis), in addition to organic contamination, also highlighted the degradation of inorganic contaminants.

In the following experiments, it was investigated how to accelerate the degradation of inorganic contaminants, especially NaCl, with a similar arrangement.

Without changing the dimensions of the diaphragm and the electrode, we changed the geometry of the cells.

The volume of the cells was reduced by half, then further, or the surface of the electrodes was increased at a given volume.

Thus, the EPTC and NaCl content of the starting solutions (EPTC and NaCl) could be broken down faster.

This was reflected in the decrease in COD of the treated solutions in the reduction of the anolyte concentration of the anolyte and in the increase of the catholyte NaOH concentration.

According to the data in *Table 1*, this is also true for real industrial wastewater. In such a device, we investigated the degradation of the organic and inorganic impurities of the diluted end lye produced by neutralizing a phosgene operating end gas, and of the effluent discharged through a centralized wastewater treatment plant.

Table 1

Real industrial wastewater electrodialysis and electrolysis

Wastewater	COD (mg/l)				Na$^+$ (g/l)			
	initial		after electrolysis		initial		after electrolysis	
	anolyte	catholyte	anolyte	catholyte	anolyte	catholyte	anolyte	catholyte
Phosgene end lye					5.55	5.55	2.3	8.8
Wastewater treatment plant effluent	123	123	88	46				

In addition to the undiluted 8.6% NaOH, concentrated diaphragm (NAFION 324 perfluoro-sulphonic acid/carboxylic acid cation selective membrane) was used to convert NaCl and Na_2CO_3 impurities in NaOH and Na_2CO_3 containing concentrated phosgene which exhibits more advantageous properties for more concentrated NaOH solutions than the NAFION 417 membrane tested. But it is also very susceptible to contamination like most membranes and diaphragms.

CONCLUSION

By the electrodialysis of aqueous solutions containing NaCl and thiolcarbamate (EPTC) contaminates both organic contamination (EPTC) and inorganic contamination (NaCl) are degradable, where end products, including SO_4^{2-} and NO_3^-, are produced from the EPTC and NaOH is produced from NaCl in the known manner.

Electrodialysis plays a role in transport processes depending on cell geometry, diaphragm and membrane and reaction parameters and affects the transport and concentration of Cl^-, Cl_2 and (Na^+OH^-) in the anolyte and catholyte.

REFERENCES

[1]   Mogyoródy, F. (2016). Study of the electrolytic degradation of organic pollutants in waste water. *Material Science and Engineering,* vol. 41 no. 1. pp. 89–95.

[2]   Seignez, S., Pulgarin, C., Péringer, P., Comninellis, C., Plattner, E. (1992). Degradation of industrial organic pollutants. Electrochemical and biological treatment and combined treatment. *Swiss Chem.*, vol. 14, no. 1, pp. 25–30.

[3]   Vidal, A., Dinya, Z., Mogyoródy, F., Mogyoródi, F. (1999). Photocatalytic Degradation of Thiocarbamate Herbicide Active Ingredients in Water. *Applied Catalysis B: Environmental,* vol. 21, no. 4, pp. 259–267.

[4]   Mogyoródy, F. (2006). Influence of Chlorine-Water Equilibria on the Electrochemical Destruction of Thiocarbamate Herbicides in NaCl Solutions. *Journal of Applied Electrochemistry*, vol. 36, no. 7. pp. 765–771.

[5]   Boxal, C., Kelsall, G. H. (1992). Hypochlorite electrogeneration. II. Thermodynamics and kinetic model of the anode reaction layer. *Icheme Symposium,* no. 127, p. 59.